

# Poisson's ratio and modern materials

G. N. Greaves<sup>1,2\*</sup>, A. L. Greer<sup>1</sup>, R. S. Lakes<sup>3</sup> and T. Rouxel<sup>4</sup>

**In comparing a material's resistance to distort under mechanical load rather than to alter in volume, Poisson's ratio offers the fundamental metric by which to compare the performance of any material when strained elastically. The numerical limits are set by  $\frac{1}{2}$  and  $-1$ , between which all stable isotropic materials are found. With new experiments, computational methods and routes to materials synthesis, we assess what Poisson's ratio means in the contemporary understanding of the mechanical characteristics of modern materials. Central to these recent advances, we emphasize the significance of relationships outside the elastic limit between Poisson's ratio and densification, connectivity, ductility and the toughness of solids; and their association with the dynamic properties of the liquids from which they were condensed and into which they melt.**

Whereas different materials respond to stress by hugely different amounts, Poisson's ratio,  $\nu$ , is contained within narrow numerical bounds, embracing the mechanical properties of every isotropic material, from the most incompressible to the most extendable, from the softest solid to the strongest liquid. Convoluting mechanical response at the atomic level with the intervening linkages to the macroscopic scale, Poisson's ratio provides a universal way to contrast the structural performance of real materials, whether homogeneous or not. Taking this wide perspective, we show how Poisson's ratio<sup>1</sup> has provided inspiration for creating new solids and liquids, and challenges in understanding existing ones. Concentrating on glasses, ceramics, polymers and metals, we review the progress made in understanding modern materials and generating new ones such as those with negative Poisson's ratios. The influence of packing and connectivity is emphasized, together with overarching relationships recently discovered between Poisson's ratio and relaxation in supercooled antecedents, and also between fracture and elasticity in the solid state. In the 200th year since the publication of Poisson's *Traité de Mécanique*<sup>2</sup> (Box 1), this is a good time to take stock of the utility of Poisson's ratio.

## Definition and physical significance

Poisson<sup>3</sup> defined the ratio  $\nu$  between transverse strain ( $e_t$ ) and longitudinal strain ( $e_l$ ) in the elastic loading direction as  $\nu = -e_t/e_l$  (Box 1). Once it was recognized that elastic moduli are independent<sup>4,5</sup>, it could be seen that the two most appropriate for formulating  $\nu$  are the isothermal bulk modulus,  $B = -VdP/dV = 1/\kappa$ , where  $\kappa$  is the isothermal compressibility, and the shear modulus  $G = \sigma_l/(2e_t)$  (ref. 6), as these are representative of the change in size and shape respectively. For isotropic materials,  $\nu$  must satisfy  $-1 \leq \nu \leq \frac{1}{2}$  (Box 2). This numerical window is illustrated in Fig. 1a where  $\nu$  is plotted as a function of  $B/G$  for a host of materials. Starting with compact, weakly compressible materials such as liquids and rubbers, where stress primarily results in shape change,  $\nu \rightarrow \frac{1}{2}$ . For most well-known solids such as metals, polymers and ceramics,  $0.25 < \nu < 0.35$ . Glasses and minerals are more compressible, and for these  $\nu \rightarrow 0$ . For gases,  $\nu = 0$ , and network structures can exhibit  $\nu < 0$  (ref. 7). Materials with negative Poisson's ratio are called 'auxetic'<sup>8</sup>. Re-entrant foams were the first reported<sup>9</sup> (Fig. 2a) but subsequently it was shown that auxeticity is a common feature of a variety of honeycomb structures and networks (Fig. 2b–d),

where  $\nu$  can take both positive and negative values, depending on orientation<sup>7,9–16</sup>, with aggregate values that can be negative. Critical fluids are the most highly compressible materials for which  $\nu \rightarrow -1$ . The huge diversity of elastic properties of modern and natural materials can also be viewed in plots of  $B$  versus  $G$  (ref. 11), as shown in Fig. 1b. This is also helpful in distinguishing ductile from brittle behaviour beyond the elastic limit (Fig. 1c).

**Nonlinear regime** The concept of Poisson's ratio can be extended into the nonlinear regime<sup>17–19</sup>, to describe elastomers such as rubbers as well as glass fibres, when subjected to gigapascal tensile stresses. Spectacular changes of  $\nu$  also occur in anisotropic auxetic materials outside the isotropic range of  $-1 \leq \nu \leq \frac{1}{2}$  at small strains. For instance,  $\nu$  was found to decrease from 0 to  $-14$  for an anisotropic expanded PTFE in a true strain range of 0.03 (ref. 17). In viscoelastic media (foodstuffs such as starch and thermoplastics such as poly(methyl methacrylate), PMMA), the mechanical response is not instantaneous or isochronal (Fig. 2e). Instead  $-e_t/e_l$  defines an apparent  $\nu$  regardless of the constitutive law that defines whether it is elastic or not. In particular,  $\nu^*(f)$  is a complex function of frequency  $f$  or a function  $\nu(t)$  of time  $t$  which can be obtained from creep and stress relaxation functions<sup>18,19</sup>. Volume and shape change processes can have different kinetics, and deformation is usually the combination of elasticity, delayed elasticity and various inelastic processes. Despite these complexities an increase of  $\nu(t)$  with time is often reported<sup>20</sup>, Poisson's ratio tending to  $\frac{1}{2}$  for most polymer materials. This can be viewed as a shift from elasticity (accompanied by volume change) to viscoelastic or even viscoplastic flow (almost volume conservative) as time passes (Fig. 2e). Conversely,  $\nu^*(f)$  decreases with increasing frequency because the elastic regime is favoured at high rates<sup>21</sup>.

**Physical significance** Materials with different Poisson's ratios behave very differently mechanically. Properties range from 'rubbery' to 'dilatational', between which are 'stiff' materials like metals and minerals, 'compliant' materials like polymers and 'spongy' materials like foams. The physical significance of  $\nu$  is revealed by various interrelations between theoretical elastic properties<sup>6</sup>. These are illustrated in the Milton map of bulk isothermal modulus  $B$  versus shear modulus  $G$  (Fig. 1b)<sup>11,22</sup>. When  $B/G \gg 1$  and  $\nu \rightarrow \frac{1}{2}$  in Fig. 1b (vertical axis), materials are extremely incompressible, like rubber,

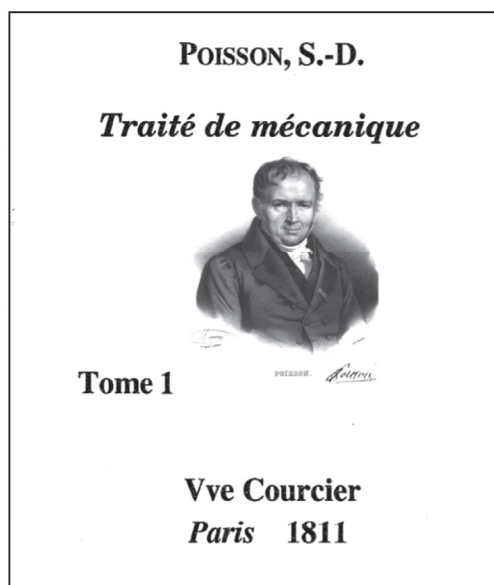
<sup>1</sup>Department of Materials Science and Metallurgy, University of Cambridge, Pembroke Street, Cambridge CB2 3QZ, UK. <sup>2</sup>Institute of Mathematics and Physics, Aberystwyth University, Aberystwyth SY23 3BZ, UK. <sup>3</sup>Department of Engineering Physics, Department of Materials Science, University of Wisconsin-Madison, Wisconsin 53706-1687, USA. <sup>4</sup>Applied Mechanics Laboratory, LARMAUR ERL-CNRS 6274, Université Rennes 1, 35042 Rennes cedex, France. e-mail: gng@aber.ac.uk

## Box 1 | Historical perspective.

Siméon Denis Poisson (1787–1840) was born in the village of Pithiviers (Loiret, France). A brilliant scholar, especially talented in mathematics, he excelled in the entrance exam for the prestigious École Polytechnique in Paris. He then devoted his life to the exploration of various fields of mathematical physics, and to solving many problems of great practical importance. Poisson's name survives in Poisson's integral, Poisson's distribution in statistics, Poisson's constant in electricity...and Poisson's ratio. In 1811 Poisson published the *Traité de Mécanique*<sup>1,2</sup>, pictured here, which remains a classical handbook in mechanics. It came in two volumes and can be found in national libraries worldwide as well as on the Internet<sup>1</sup>.

An analysis of the shape and volume changes of a fluid under arbitrary loading is introduced in the second volume<sup>2</sup>. However,

it was only in 1827 that Poisson<sup>3</sup>, starting from an explicit molecular interaction hypothesis formulated several years earlier by the French engineer and physicist Navier, proposed an expression (see right-hand image) for the change in cross-sectional area ( $\delta S/S = -\beta$ ) stemming from the elongation ( $\delta L/L = e$ ) of an elastic wire and suggested that  $\beta = e/2$ . As  $\beta = 2\nu e$ , so  $\nu = 1/4$ . Poisson considered this result as being in perfect agreement with nature based on an experiment conducted on a brass rod ( $\nu \approx 0.357$ ) by his contemporary Cagniard de Latour. But it became clear, first through Cauchy in his *Exercices de Mathématiques*<sup>4</sup> and later especially after the experiments performed by Voigt<sup>5</sup>, that two independent moduli of elasticity are necessary to characterize the elastic behaviour of isotropic materials<sup>6</sup>. Accordingly  $\nu$  must differ from one material to another, even crystalline materials in the same class.



## NOTE sur l'Extension des Fils et des Plaques élastiques.

PAR M. POISSON.

Soit  $a$  la longueur d'un fil élastique qui ait partout la même épaisseur; soit  $b$  l'aire de la section normale à sa longueur, et par conséquent  $ab$  son volume. Supposons qu'on lui fasse subir une petite extension, de sorte que sa longueur devienne  $a(1+\alpha)$ ,  $\alpha$  étant une très-petite fraction; en même temps le fil s'amincira; et si nous désignons par  $b(1-\epsilon)$  ce que deviendra l'aire de la section normale,  $\epsilon$  étant aussi une très-petite fraction, son nouveau volume sera à très-peu près  $ab(1+\alpha-\epsilon)$ . Or, d'après la théorie des corps élastiques que j'exposerai dans un prochain Mémoire, on doit avoir :

$$\epsilon = \frac{1}{2}\alpha;$$

d'où il résulte que par l'extension  $\alpha$  d'un fil élastique, son volume se trouve augmenté, suivant le rapport de  $1+\frac{1}{2}\alpha$  à l'unité, et sa densité diminuée suivant le rapport inverse.

Ce résultat s'accorde parfaitement avec une expérience que M. Cagniard-Latour a communiquée récemment à l'Académie, et dont voici la description.

most liquids and also granular solids. When  $B/G \ll 1$  and  $\nu \rightarrow -1$  in Fig. 1b (horizontal axis), materials are extremely compressible, examples being re-entrant foams and molecular structures<sup>7,11,14,16,23,24</sup>. Most common materials fall in between these extremes. Materials possessing stiff arms or struts in directions normal to the loading axis, such as honeycomb structures loaded along the  $c$  axis, will resist transverse contraction and exhibit  $\nu \approx 0$  as cork does (Fig. 2d) or  $\nu < 0$  as some zeolites might (Fig. 2b)<sup>25</sup>. For ceramics, glasses and semiconductors,  $B/G \approx 5/3$  and  $\nu \rightarrow 1/4$  (refs 26–29). Likewise, metals are stiff<sup>6,30,31</sup>,  $B/G$  ranging from 1.7 to 5.6 and  $\nu$  from 0.25 to 0.42 (ref. 32; Fig. 1c). In sharp contrast, polymers are compliant and yet they share similar values: that is,  $B/G \approx 8/3$  and  $\nu \approx 0.33$  (refs 18–20), the difference relating to the magnitude of the elastic moduli, decades smaller than for inorganic materials (see Fig. 5).

Through the elastic moduli, Poisson's ratio can also be expressed in terms of the transverse (shear) and longitudinal (compressive) speeds of sound,  $V_t$  and  $V_l$  respectively<sup>6</sup> (Box 2). These speeds and their ratio are pertinent to seismic waves studied in geophysics<sup>26</sup>. In condensed matter, where  $V_t$  and  $V_l$  can be measured by Brillouin scattering or shock wave experiments, Poisson's ratio can be followed through abrupt changes in mechanical properties. For example, when metals melt,  $\nu$  increases from  $\sim 0.3$  to 0.5

(refs 33–37). During the collapse of microporous crystals,  $\nu$  rises from directionally auxetic values<sup>15,25</sup> to isotropic values of 0.2 typical of many glasses<sup>38</sup>. With densification Poisson's ratio for glasses continues to rise, for silica increasing from 0.19 to 0.33 (ref. 39; see Fig. 5d).

## Poisson's ratio and materials

**Poisson's ratio and packing density** Poisson's ratio is intimately connected with the way structural elements are packed. For gold or platinum-based bulk metallic glasses, for example, which represent some of the densest metals because of the variety of atom sizes,  $\nu \rightarrow 1/2$ . Crystalline metals are less densely packed, typified by hard metals like steel for which  $\nu \approx 1/3$ . By contrast, the density of covalent solids is less and so is Poisson's ratio. Finally, auxetic materials have dilational re-entrant architecture and  $\nu < 0$ .

This correlation between  $\nu$  and atomic packing density  $C_g$  has only recently been recognized (Fig. 3) because it is rather difficult to define in complex solids. Concomitant effects, like temperature and pressure, also sometimes obscure the underlying structural effect. The case of pure crystalline substances seems particularly complicated. At first sight Poisson's ratio tends to increase with the atomic packing density so that  $\nu_{cd} < \nu_{bcc} < \nu_{fcc,hcp}$  (where cd, bcc, fcc

**Box 2 | Poisson's ratio, Angell plot, non-ergodicity and terahertz vibrations.****Defining Poisson's ratio**

Poisson's ratio  $\nu$  compares the strains in the transverse  $e_i$  and longitudinal  $e_l$  directions under uniaxial stress:  $\nu = -e_i/e_l = -(\Delta D/D)/(\Delta L/L)$  (panel a)<sup>6</sup>. For isotropic materials,  $\nu$  can be expressed in terms of the bulk modulus  $B$  and the shear modulus  $G$ , which relate to the change in size and shape respectively:  $\nu = [3(B/G - 2)]/[6(B/G + 2)]$  (ref. 26). This defines numerical limits for Poisson's ratio,  $-1 \leq \nu \leq 1/2$  for  $0 \leq B/G < \infty$ . Poisson's ratio can also be written in terms of the longitudinal and transverse speeds of sound,  $V_l$  and  $V_t$ , respectively<sup>26</sup>:  $\nu = [1/2(V_l/V_t)^2 - 1]/[(V_l/V_t)^2 + 1]$ . Alternatively<sup>33</sup>,  $\nu = [3 - (V_l/V_B)^2]/[3 + (V_l/V_B)^2]$  where  $V_B = \sqrt{B/\rho}$ , the so-called bulk speed, which is directly measured in liquids, where  $\nu = 1/2$  and  $V_t = 0$ . For examples and demonstrations, see <http://silver.neep.wisc.edu/~lakes/Poisson.html>.

**Melt fragility**

Panel b shows an Angell plot,  $\log \eta$  versus  $T_g/T$ , of glass-forming liquids<sup>108</sup> where  $\eta$  is the shear viscosity and  $T_g$  the glass transition. The glass transition is defined by  $\eta(T_g) = 10^{12}$  Pa for all glass-forming liquids. From the Maxwell viscosity relation ( $\eta = G_\infty \tau$ )<sup>79</sup> the Angell plot can also be expressed as a function of structural relaxation time  $\tau$ :  $\log \tau$  versus  $T_g/T$ . Because for many supercooled materials the instantaneous shear modulus  $G_\infty$  lies in the range 10 to 30 GPa, the glass transition can also be defined by  $\sigma(T_g) \approx 100$  s. The melt fragility is defined by  $m = [\partial \log \eta, \tau(T)/\partial(T_g/T)]_{T=T_g}$ , which distinguishes strong liquids like silica ( $m \approx 20$ ) from fragile liquids like PMMA ( $m \approx 118$ ) at  $T_g$ . At the melting temperature  $T_m$ , which is typically related to the glass transition  $T_g$  by  $T_m/T_g \approx 3/2$ , the viscosities of strong and fragile liquids can differ by many orders of magnitude, directly affecting the viscoelastic timescale of melting. Examples of  $m$  changing from strong to fragile liquids with compression are shown in Fig. 8c and d.

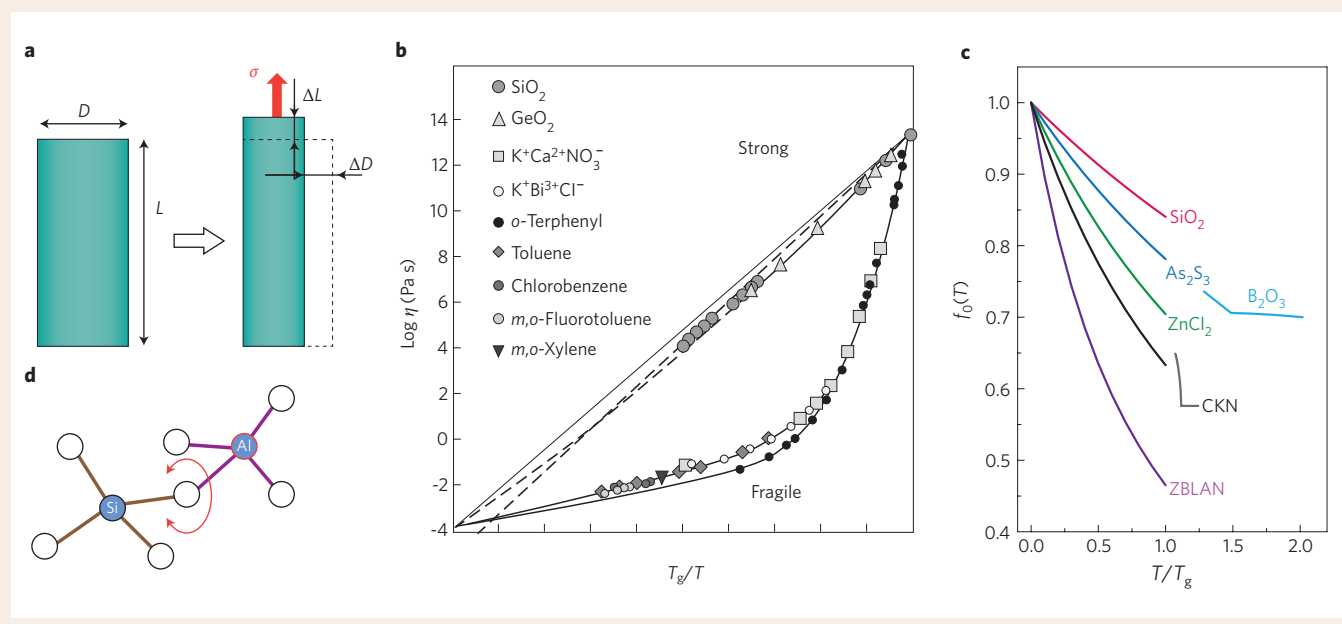
**Non-ergodicity in supercooled liquids and glasses**

The non-ergodicity factor  $f_0$  versus  $T/T_g$ , which is measured in Brillouin and inelastic X-ray scattering<sup>113</sup>, records the

departure from thermodynamic equilibrium and increases from the supercooled liquid to the glass as the temperature falls (panel c; CKN is  $K^+Ca^{2+}NO_3^-$ )<sup>79</sup>. In particular,  $f_0 = (1 - \alpha T/T_g)^{-1}$ , where  $\alpha$  is a constant<sup>105,106</sup>. The factor  $f_0$  is a measure of the magnitude of density fluctuations present at a given temperature and to a first approximation<sup>100</sup>  $f_0 \approx (V_l/V_t)^2 = 3G/(4G + 3B)$ . It follows that  $\alpha \propto B/G$ , in which case  $\alpha$  scales with Poisson's ratio as both scale with  $m$ . Figure 7b illustrates empirically  $m$  versus  $\alpha$  for a variety of organic and molecular glass-forming liquids with a wide range of fragilities.

**Terahertz vibrations and the boson peak**

Terahertz vibrations, measured directly by inelastic neutron scattering, are typified by librational modes that characterize the dynamics of tetrahedral glasses and microporous crystals<sup>94</sup>, as illustrated in panel d. These dynamics are embraced by the boson peak<sup>79</sup> illustrated in Fig. 8a and b. For glasses in general, the intensity of the boson peak  $A_{BP}$  is governed by the statistical fluctuations in density, which are related in turn to the elastic moduli<sup>101</sup>:  $A_{BP} \propto G/B$ . Accordingly, from panel a, the size of the Boson peak at a given temperature is reciprocally related to Poisson's ratio and empirically to the parameter  $\alpha$  from panel c, which is inversely related to the non-ergodicity factor  $f_0$ . From Fig. 7a and b,  $A_{BP}$  must also be inversely related to the melt fragility  $m$ , which (from panel b) can differ by **an order** of magnitude, from the strongest to the most fragile glass-forming liquids. Furthermore, from Fig. 1c and 7c,  $A_{BP}$  for a glass decreases as the fracture energy increases, distinguishing brittle from ductile materials. Glasses obtained from strong liquids are the most brittle and have the largest boson peaks. Conversely, boson peaks are smallest in glasses quenched from fragile liquids. Broadly speaking, terahertz vibrations drive the dynamics of glass formation and phase transformations<sup>94</sup> (Fig. 5)—including melting. Figure adapted with permission from: panel b, ref. 107, © 2001 NPG; panel c, ref. 79, © 2007 Taylor & Francis.



and hcp stand for cubic-diamond, body-centred cubic, face-centred cubic and hexagonal close-packed crystalline structures respectively). Moreover, for a given crystalline structure and valence,  $\nu$  mostly increases with atomic number  $Z$ , and indeed the electronic

band structure and the valence electron density come into play. This is exemplified for the case of metals with high electrical conductivity, such as copper, silver and gold, which also have high Poisson's ratio (Figs 1c and 3).

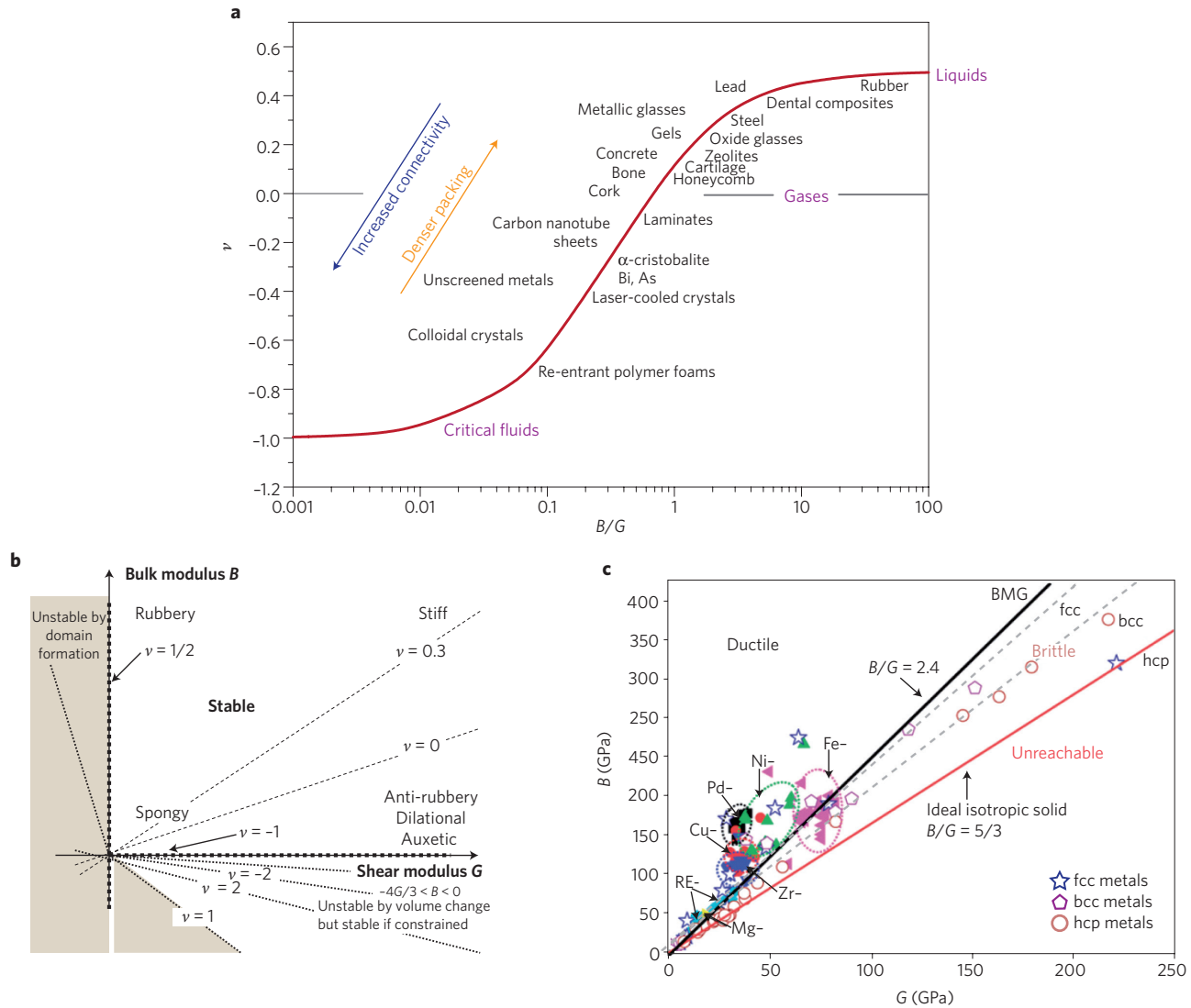


**Figure 1 | Poisson's ratio: physical significance, materials characteristics and the Milton map.** **a**, Numerical window of Poisson's ratio  $\nu$ , from  $-1$  to  $1/2$ , plotted as a function of the ratio of the bulk and shear moduli  $B/G$  for a wide range of isotropic classes of materials (see text for details). **b**, Milton map<sup>11</sup> of bulk modulus versus shear modulus, showing the regimes of  $\nu$ , and the differences in material characteristics. The stability boundaries are pertinent to phase transformations<sup>11,12</sup>. **c**, Jiang and Dai plot<sup>32</sup> of bulk modulus versus shear modulus for metallic glasses and polycrystalline metals. Straight lines refer to thresholds for brittle-ductile transition in metals. The ratio  $B/G = 5/3$  ( $\nu = 0.25$ ) relates to the lower limit of Poisson's ratio for most metals. RE, rare earth. Ni- indicates nickel-based, and so on. Figure adapted with permission from: **a**, ref. 11, © 1992 Elsevier; ref. 12, © 1993 Wiley; **c**, ref. 32, © 2010 Taylor & Francis.

Considering polycrystalline solids, these are macroscopically isotropic and have Poisson's ratios of  $\nu_C(0.2) < \nu_{Si}(0.22) < \nu_{Ge}(0.278)$  for tetravalent elements, and for the hcp polymorphs of  $\nu_{Zn}(0.25) < \nu_{Cd}(0.3)$  or  $\nu_{Ti}(0.32) < \nu_{Zr}(0.36) < \nu_{Hf}(0.37)$ , just to mention a few. Lead ( $\nu_{Pb} = 0.44$ ) and thallium ( $\nu_{Tl} = 0.45$ ) with high  $Z$  have remarkably high Poisson's ratios. In the case of crystalline structures, the valence electron density plays a key role, and *ab-initio* calculation is becoming an increasingly popular approach following the early work of Cohen<sup>27</sup>. Subsequently, the cases of diamond semiconductors ( $\nu_{Si} = 0.22$  and  $\nu_{Ge} = 0.28$ ) were reported<sup>28</sup>, as were the fullerenes<sup>29</sup>, molybdenum<sup>40</sup> and most recently dental amalgams<sup>41</sup>. There are, however, isolated cases where the interpretation is not straightforward. Most data are measured under ambient conditions, whereas  $\nu$  is known to generally increase with temperature (see Fig. 4b). High melting points thus favour low Poisson's ratio (everything else remaining unchanged) and vice versa. This is possibly why tungsten, being more refractory than molybdenum, has a smaller Poisson's ratio and why beryllium, combining low  $Z$  with a

comparatively high melting point (1,560 K), exhibits a remarkably small Poisson's ratio of 0.032 and is also very brittle.

Paradoxically, complex materials such as polycomponent glasses follow simple monotonic trends. In this case the atomic packing density  $C_g$  is defined as the ratio between the minimum theoretical volume occupied by the ions and the corresponding effective volume of the glass (Fig. 3). For instance,  $C_g$  is about 0.52 for a standard window glass and 0.45 for silica glass. An estimation of the packing density in metallic glasses can be obtained using the atomic radii of the corresponding constituent metals. Poisson's ratio, which covers a wide range for inorganic glasses, increases almost monotonically with  $C_g$  (Fig. 3). Eventually, within limited compositional ranges, linear trends can be observed<sup>42</sup>. Much earlier, Makishima had proposed that  $\nu = 1/2 - 1/7.2C_g$  for silicate glasses<sup>43</sup> but without knowledge of accurate atomic glass network parameters, such as interatomic distance and coordination number.

Nevertheless, a direct comparison of Poisson's ratio for specimens of identical composition and initial structure but submitted

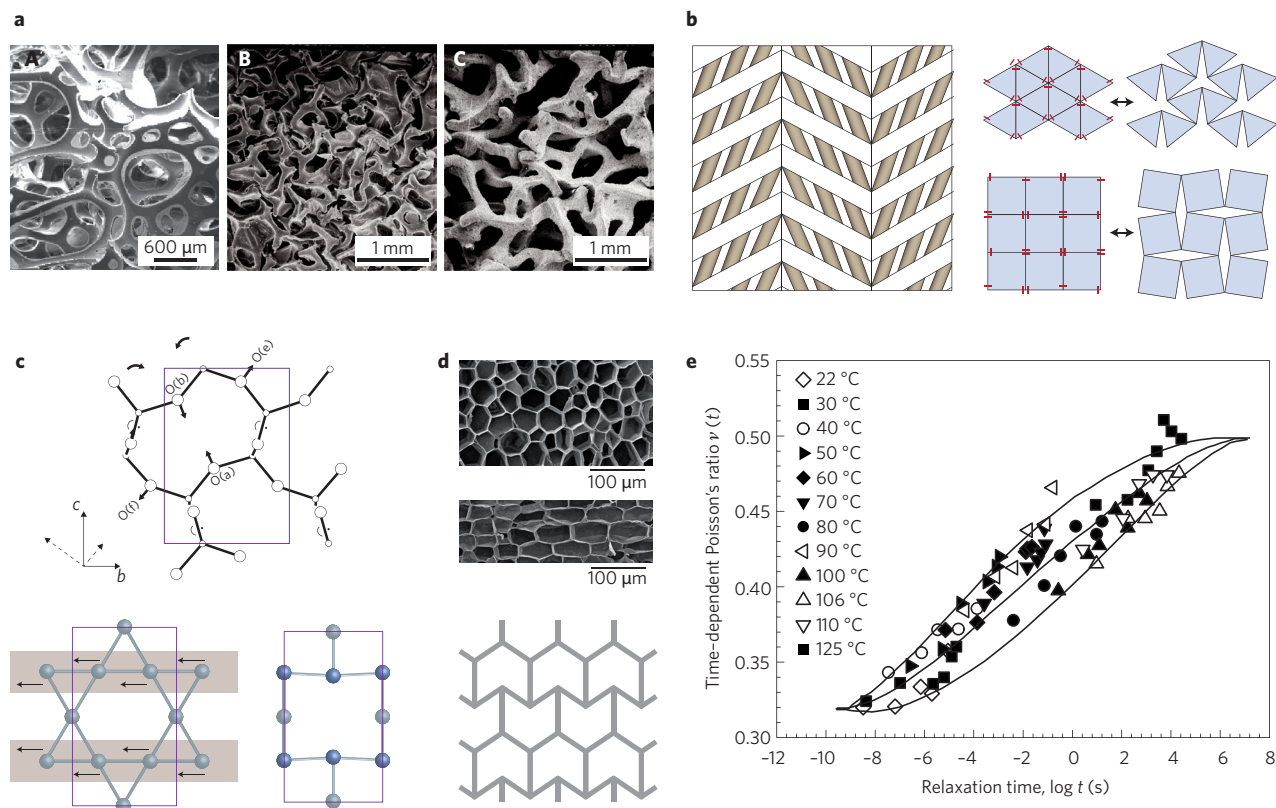


**Figure 2 | Varying Poisson's ratio structurally.** **a**, Foams: conventional polyurethane foam with  $\nu \approx 0.3$  (A). Negative Poisson's ratio foam with folded-in (re-entrant) cells fabricated from polyurethane foam (B) and from copper foam (C), after Lakes<sup>9</sup>. Figure adapted with permission from ref. 9, © 1987 AAAS. **b**, Auxetic geometries: hierarchical laminate (left), after Milton<sup>11</sup>. Rotating hinged triangle and square structures (right) after Grima *et al.*<sup>25,64</sup>. Left panel adapted with permission from ref. 11, © 1992 Elsevier; right panel reproduced with permission from ref. 64, © 2005 Wiley. **c**, Atomic motifs: crystal structure of  $\alpha$ -cristobalite projected along the  $a$  axis (upper), after Haeri *et al.*<sup>7</sup>. Under compression the bridging oxygen pairs on opposite sides of the six-fold ring —  $a$  and  $b$ ,  $c$  and  $d$ ,  $e$  and  $f$  — move conversely through tetrahedral rotations as shown. Changing geometry of silver atoms in the van der Waals solid  $\text{Ag}_3[\text{Co}(\text{CN})_6]$  (lower), showing the formation of a re-entrant honeycomb under 0.23 GPa pressure<sup>75</sup>.  $\text{Co}(\text{CN})_6$  anions occupy adjacent interstitial locations and the arrows indicate the action underlying the displacive transition. Figure reproduced with permission from: Top panel, ref. 7, © 1992 AAAS; bottom panels, ref. 75, © 2008 NAS. **d**, Cellular structures: honeycomb structure found in cork<sup>66</sup> normal to the direction of growth (upper) where  $\nu \leq 0$  and parallel to this (middle) where  $\nu > 0$ . Semi-re-entrant honeycomb structure proposed to model zero Poisson's ratio materials (lower)<sup>67</sup>. Figure reproduced with permission from: Top panel, ref. 66, © 2005 Maney; bottom panel, ref. 67, © 2010 Wiley. **e**, Time-dependent Poisson's ratio for poly(methyl methacrylate), PMMA, showing the gradual rise in  $\nu(t)$  with relaxation under uniaxial shear from the instantaneous elastic value of 0.33 to the viscoelastic and eventual incompressible bulk value of 0.5. Figure reproduced with permission from ref. 20, © 1997 Wiley.

to treatments affecting the packing density (isostatic pressing, agitation, annealing to promote structural relaxation) provides clear evidence for a sensitive increase of  $\nu$  in most cases<sup>39,44,45</sup>. For example, for silica glass this lies between 0.15 and 0.19 under ambient conditions. After treatments under high pressure (typically above 10 GPa),  $\nu$  increases to 0.25 (ref. 46), reaching 0.33 above 30 GPa (ref. 39; see Fig. 5d), the effect of densification depending on the initial  $\nu$  value<sup>47</sup>. The same situation is observed with sand: for loose sand  $\nu$  is typically around 0.2 whereas dense sand reaches 0.45 and saturated cohesive soils are almost incompressible ( $\nu = 0.5$ )<sup>48</sup>. The increase of  $\nu$  with  $C_g$  is observed either along elastic loading paths or after permanent densification<sup>46</sup>. A direct manifestation of the correlations between  $\nu$  and  $C_g$  (Fig. 3) and densification<sup>47</sup> concerns the way matter deforms under high contact pressure, such as during indentation or scratch loading<sup>46</sup>. For low- $C_g$  materials (vitreous silica and porous materials), there is sufficient free volume for densification to occur so that the stress is accommodated by the collapse of matter beneath the contact area. For high- $C_g$  materials (precious metals, metallic glasses, clay), deformation is nearly isochoric or involves some dilation, and proceeds by localized shear (Fig. 6)<sup>46,49–51</sup>. Deformation during indentation is mainly a projection of elastic behaviour before reaching the yield point.

Materials with small Poisson's ratio are more easily compressed than sheared (small  $B/G$ ), whereas those with high Poisson's ratio resist compression in favour of shear (large  $B/G$ )<sup>46</sup>. The ability of a material to dissipate the elastic loading energy by any permanent deformation mechanism ultimately governs its cracking resistance. Indeed the brittle–ductile transition in terms of  $\nu$  is striking—particularly in metals (Fig. 7c).

**Connectivity and temperature** High packing density is incompatible with structures that are highly connected; consider the random packing of balls (0D) versus rods (1D) or polyhedral frames (2D and 3D) in a box. Judging from the correlation with  $C_g$  (Fig. 3),  $\nu$  is expected to decrease with increasing connectivity (Fig. 4a), not least because stiff arms in cross-linked structures oppose transverse contraction upon tensile loading. The relatively low values of  $B/G$  and hence  $\nu$  for diamond, fullerite and hard materials in general (Fig. 3) is an indication of the high degree of directional covalent bonding. In the case of glasses, the degree of cross-linking of the atomic network built on glass-forming elements can be used as a first approach, in lieu of an accurate description based on the electron band structure.

For glasses with covalently bonded atoms the mean coordination number  $\langle n \rangle$  is a useful index of the connectivity (Fig. 4a). For

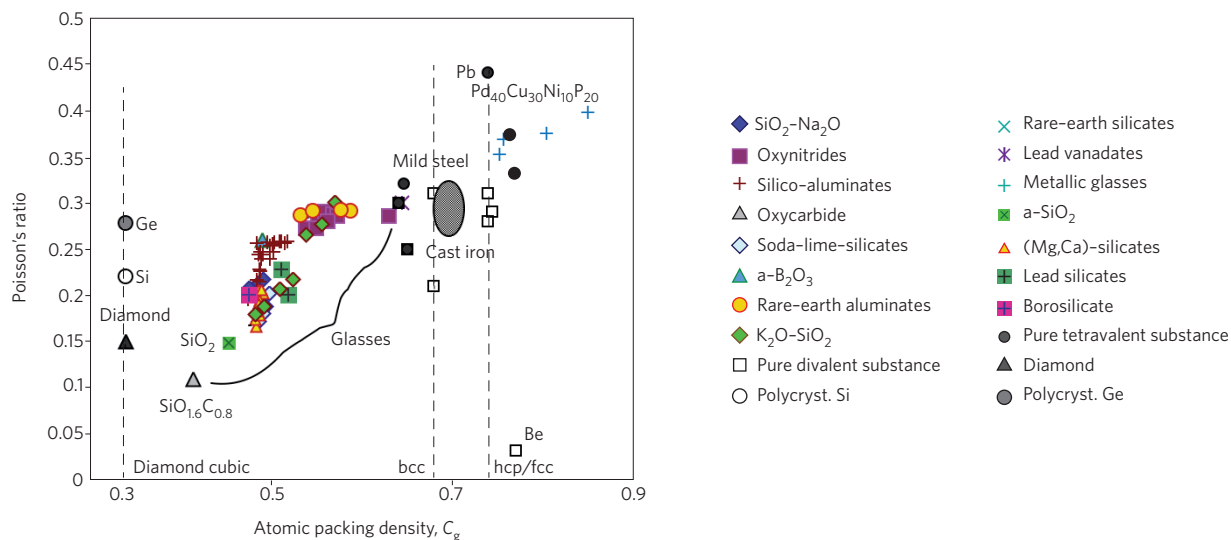


**Figure 3 | Poisson's ratio and atomic packing.** Poisson's ratio  $\nu$  as a function of the atomic packing density  $C_g = \rho \sum f_i V_i / \sum M_i$ , where  $\rho$  is the specific mass,  $N$  is Avogadro's number,  $r_A$  and  $r_B$  are the ionic radii,  $f_i$  is the molar fraction and  $M_i$  is the molar mass. For the  $i$ th constituent with chemical formula  $A_x B_y$ ,  $V_i = (4/3) \pi N (x r_A^3 + y r_B^3)$ . The distinct symbols show that there are monotonic and nearly linear increases of  $\nu$  with  $C_g$  for each separate chemical system<sup>42</sup>. Figure adapted with permission from ref. 42, © 2007 Wiley.

example, for a  $\text{Ge}_x\text{Se}_{1-x}$  ( $x < 1$ ) glass,  $\langle n \rangle = 2(x + 1)$ . Provided  $\langle n \rangle$  is less than 2.1, the volume fraction of Ge-containing chains is negligible so that deformation essentially proceeds through the alignment of chains, with elastic properties expected to be dominated by weak inter-chain van der Waals forces, analogous to polymeric materials. Accordingly shear resistance is small and  $\nu$  large. As  $\langle n \rangle$  increases, covalent bonds come into play and a three-dimensional network builds up, leading to a significant decrease in  $\nu$ . For oxide glasses, the number of bridging oxygen atoms,  $n_{\text{BO}}$ , per glass-forming cation (Si, Al, Zr, As, B, P and so on) provides a straightforward estimation of network crosslinking, where BO refers to bridging oxygens. For pure oxide glasses such as  $\text{As}_2\text{O}_3$ ,  $\text{B}_2\text{O}_3$  and  $\text{P}_2\text{O}_5$ ,  $n_{\text{BO}} = 3$  and  $\nu \approx 0.3$ , whereas for  $\text{a-SiO}_2$  and  $\text{a-GeO}_2$ ,  $n_{\text{BO}} = 4$  and  $\nu \approx 0.2$ . Nuclear magnetic resonance measurements lead mostly to experimental  $n_{\text{BO}}$  values that are very close to the theoretical ones. It should be emphasized, though, that  $\langle n \rangle$  and  $n_{\text{BO}}$  are not equivalent. For instance, in the case of  $\text{a-SiO}_2$ ,  $\langle n \rangle = 2.67$  whereas  $n_{\text{BO}} = 4$ . Highly crosslinked networks, such as silica glass, lead to small Poisson's ratios (0.19), whereas weakly correlated networks, such as chain-based chalcogenide glasses or cluster-based metallic glasses, show values between 0.3 and 0.4 (Fig. 4a)<sup>42</sup>. Hence, as already noticed by Bridge and Higazy<sup>52</sup> in a study limited to some oxide glasses, and by Sreeram *et al.*<sup>53</sup> for chalcogenide glasses and later generalized by Rouxel<sup>42</sup> for a wide range of glasses including covalent and metallic ones,  $\nu$  depends almost linearly on connectivity and increases as the dimensionality of the structural units decreases.

Extreme cases are illustrated on the one hand by silicon oxycarbide glasses, where the formation of  $\text{CSi}_4$  tetrahedra based on fourfold covalent carbon atoms further enhances the network cross-linking over that of  $\text{a-SiO}_2$ , with  $\nu$  reaching 0.11 for the polymer-derived  $\text{SiO}_{1.6}\text{C}_{0.8}$  composition<sup>54</sup>. On the other hand, for precious-metal-based metallic glasses, which are considered to consist of quasi-equivalent cluster-type units (0D) eventually packed with icosahedral-like medium range order<sup>55,56</sup>,  $\nu$  approaches 0.4. Judging from a Poisson's ratio of 0.3, the glassy ice network might be based on chain-like hydrogen-bonding of water molecules or contain cluster-like structural units, for example icosahedral clusters as suggested by Hessinger *et al.*<sup>57</sup>. However, diffraction studies of low-density amorphous (LDA) ice reveal a hydrogen-bonded tetrahedral network mainly comprising sixfold rings<sup>58</sup>, rather like water. With the application of pressure, crystalline hexagonal ice

transforms into high-density amorphous (HDA) ice<sup>59</sup>. This differs from LDA ice by the presence of interstitial molecules<sup>58</sup> that interrupt the network topology.

The material composition, however, is insufficient to interpret the observed correlation between  $\nu$  and the connectivity. Temperature comes into play. This is because elastic properties are very sensitive to temperature and  $\nu$  is expected to increase in crystalline materials as the melting point ( $T_m$ ) is approached or in glasses above the glass transition temperature ( $T_g$ ) (Fig. 4b and 5c). A steep increase in Poisson's ratio reveals rapid network depolymerization, as is the case for organic chain polymers such as glycerol or polystyrene and also for  $\text{a-B}_2\text{O}_3$  (ref. 42) which transform into fragile liquids (Box 2). In cellular materials, such as open-cell foams, the reduction of the volume fraction of solid ( $\phi$ ) weakens the interconnections favouring bending with respect to axial deformation, analogous to an increase of temperature in dense solids. Indeed the analysis of foam structures<sup>60</sup> predicts that  $\nu$  increases as  $\phi$  decreases. For glasses like silicates and aluminosilicates forming strong liquids above  $T_g$  (Box 2),  $\nu$  increases far more slowly (Fig. 4b).

In the face of this complexity, we note that glasses offer a unique opportunity to tune the composition smoothly to change the packing density and/or the connectivity. One can hence produce glasses with Poisson's ratio *à la carte*.

**Auxetic materials** The theory of elasticity allows values of Poisson's ratio for isotropic solids down to  $-1$  (Fig. 1a). Although for years the possibility of negative  $\nu$  was excluded<sup>61</sup>, re-entrant foams (Fig. 2a) achieved values as negative as  $-0.8$  (refs 9–13). Fabricated under pressure, they are isotropic if compression is triaxial or anisotropic under extrusion conditions. They have been called 'anti-rubber' because they are opposite in elastic response to rubber (Fig. 1b). The effect in foam or honeycomb occurs by the unfolding of re-entrant cells as they are stretched (Fig. 2a). By contrast in typical foams, the cells are convex so their deformation gives rise to a 'normal' positive Poisson's ratio. A coarse cell structure is not required to predict a positive or negative Poisson's ratio; classical elastic properties have no length scale<sup>62</sup>. Rigid mechanical models, such as rotating hinged squares and triangles, replicate auxetic behaviour and serve as models for molecular structures and designs (Fig. 2b)<sup>7,8,25,63,64</sup>. It is not necessary to have empty space in a microstructure to achieve the effect: hierarchical two-phase laminates with a chevron structure and

multiple length scales can approach the isotropic lower limit  $\nu = -1$  (ref. 11). These microstructures are played out in the  $\alpha$ -cristobalite network (Fig. 2c). Microstructures such as composites with rotating discs and units, magnetic films, hypothetical granular structures or plasmas in neutron stars can also exhibit such effects<sup>24,64,65</sup>.

Negative Poisson's ratio can result in enhanced toughness. The mode I (opening) fracture stress of a structure from a pre-existing flaw is proportional to  $\sqrt{[\gamma E/a(1 - \nu^2)]}$ , where  $\gamma$  is the fracture surface energy,  $E$  is Young's modulus, and  $a$  is the critical flaw size. For Poisson's ratio approaching  $-1$ , the material is expected to become very tough. Likewise it should resist indentation as the contact surface area is proportional to  $(1 - \nu^2)/E$ . Even if the

material is compliant, provided  $\nu$  is close to the thermodynamic limit of  $-1$  (Fig. 1b), it will be difficult to indent. Other anticipated enhancements include improved shear stiffness, self-adaptive vibrational damping and shock absorption, with applications in body armour, increased-sensitivity piezoelectric composites, fibre composites with greater pull-out resistance, a natural tendency to form dome-shaped surfaces (synclastic curvature), foams with improved filter performance and drug release, more comfortable textiles with reduced clothing pressure and so on<sup>8,25,64</sup>.

**Anisotropic behaviour** Anisotropic materials, including crystals and fibrous composites, have directional elastic properties where  $\nu$

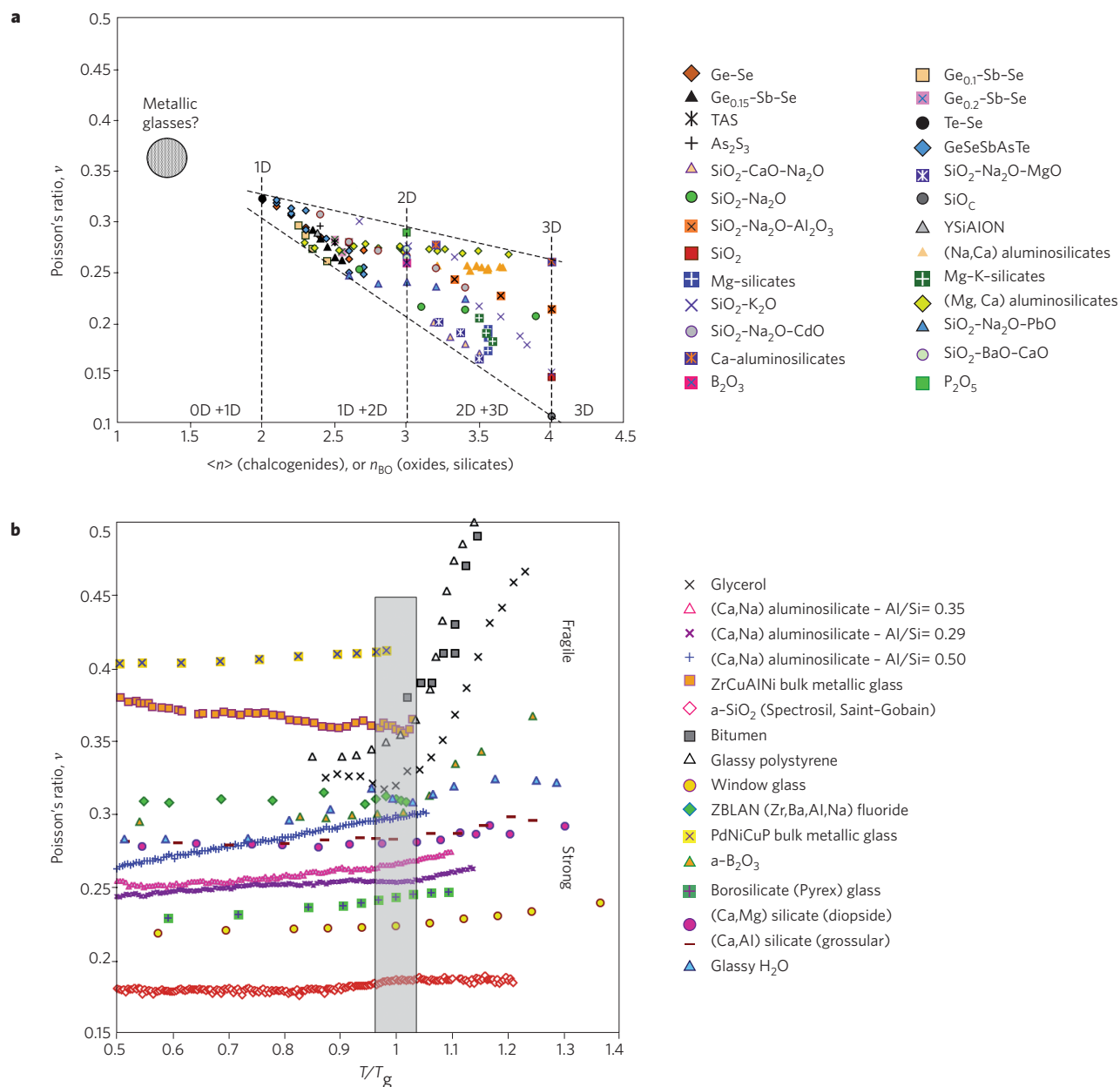


**Figure 4 | Connectivity in glasses and liquids.** Poisson's ratio  $\nu$  in glasses and liquids reflects their structure and its dependence on temperature. **a**, In glasses  $\nu$  varies with the average coordination number  $\langle n \rangle$  in chalcogenide glasses, or the number of bridging oxygens per glass-forming cation  $n_{BO}$  in oxide glasses (ref. 42).  $\langle n \rangle$  is defined as  $\langle n \rangle = \sum f_i n_i$ , where  $f_i$  and  $n_i$  are, respectively, the atomic fraction and the coordination number of the  $i$ th constituent, and  $n_{BO} = 4 - \sum M_i z_i / \sum F_j$ , where  $M_i$  and  $z_i$  are respectively the atomic fraction (after deduction of the number of charge compensators) and the valence of the  $i$ th modifying cation, and  $F_j$  is the fraction of the  $j$ th glass-forming cation. **b**, The temperature dependence of  $\nu$  for different glass-forming systems. The vertical bar marks the glass transition temperature  $T_g$ , above which sharp rises are observed, particularly for fragile supercooled liquids<sup>42</sup>. Figure reproduced with permission from ref. 42, © 2007 Wiley.

can be negative, leading to unusual or extreme behaviour as well as coupling between stretch and shear or bend and twist. Carbon nanotube sheets<sup>16</sup>, for example, exhibit in-plane auxeticity. By contrast, cork has an anisotropic cellular structure (Fig. 2d). If tensile stress is applied normal to the radial growth,  $\nu \leq 0$  in the direction of growth and  $\nu > 0$  orthogonal to this<sup>66</sup>. By alternating entrant and re-entrant honeycomb layers, Grima *et al.* have shown how structures with  $\nu \approx 0$  can be generated in particular directions, leading to cylindrical shaped curvatures<sup>67</sup>.

Directional auxetic properties were originally envisaged by Saint-Venant<sup>68</sup> for anisotropic materials and later by Lempriere<sup>69</sup> for composites. In inorganic materials, anisotropic auxetic behaviour was suggested for iron pyrites<sup>6</sup> with  $\nu = 1/7$  in some directions. Arsenic, antimony and bismuth<sup>70</sup> are highly anisotropic in single-crystal form and their calculated Poisson's ratios are negative in some directions. In  $\alpha$ -cristobalite, Poisson's ratios range from +0.08 to -0.5, depending on direction (Fig. 2c)<sup>71</sup>, with an aggregate expected to be negative<sup>25</sup>. Many cubic metals when stretched in the [110] direction become auxetic<sup>14</sup>. Likewise, many zeolites show off-axis swings in  $\nu$  on rotation<sup>15,25</sup>. Influenced by the presence of extra-framework water and also templating molecules, recent calculations predict

oscillations in  $\nu$  of 0.5 to -0.5 for 45° rotations<sup>72</sup>. Such anisotropic auxetic behaviour might well influence adsorption chemistry, if crystals are stressed along specific directions<sup>25,73</sup>.

Broadly speaking, extreme Poisson's ratios in single crystals are found to be strongly correlated with elastic anisotropy<sup>74</sup>. For example, in  $\text{Ag}_3[\text{Co}(\text{CN})_6]$  the metals form an alternate layered structure containing auxetic motifs (Fig. 2c) which expands along the *c* axis but contracts in the basal plane under isotropic compression<sup>75</sup>: that is, the compressibility  $\kappa$  has different signs in different crystallographic directions. This behaviour is also expected to be associated with anisotropic Grüneisen parameters, whereby negative linear compressibility in specific directions should be accompanied by negative thermal expansion, which is also observed<sup>76</sup> and is huge compared with related compounds like  $\text{H}_3[\text{Co}(\text{CN})_6]$ ,  $\text{ZrW}_2\text{O}_8$  or  $\text{Cd}(\text{CN})_2$  (ref. 77).

**Poisson's ratio during phase transformations**

At different temperatures and pressures, crystalline materials can undergo phase transitions<sup>78</sup> and, attracting considerable debate, so too can glasses and liquids<sup>58,79-81</sup>. Whenever a phase boundary is crossed or criticality is approached, the isothermal compressibility

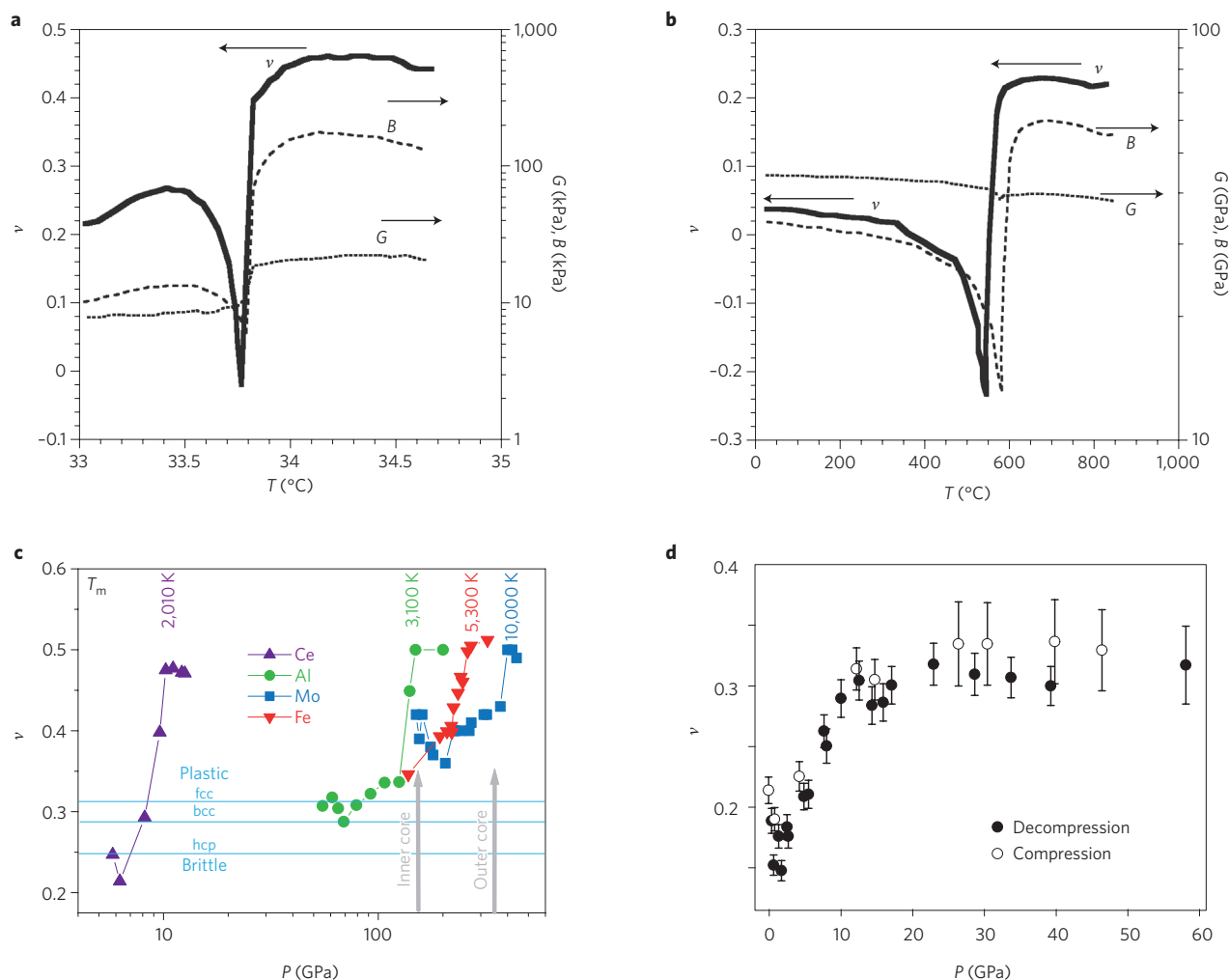


**Figure 5 | Poisson's ratio and phase transformations.** **a**, Bulk modulus  $B$ , shear modulus  $G$  and Poisson's ratio  $\nu$  of a polymer gel versus temperature associated with a volume phase transition close to a critical point measured optically<sup>82</sup>. **b**, Bulk modulus, shear modulus and Poisson's ratio associated with the  $\alpha$ - $\beta$  first-order transition in quartz versus temperature, measured with resonant ultrasound spectroscopy (RUS)<sup>84</sup>. **c**, Melting of metals at ultra-high temperatures and pressures. Poisson's ratio of cerium<sup>97</sup>, aluminium<sup>88</sup>, iron<sup>36</sup> and molybdenum<sup>34,35</sup> versus pressure during shock-melting experiments, with the incipient melting temperatures  $T_m$  indicated. The outer and inner pressure limits of the Earth's core are indicated as is the brittle-ductile threshold from Fig. 1c and Fig. 7c. **d**, Poisson's ratio of silica glass during compression and decompression measured with Brillouin scattering<sup>39</sup>. Figure reproduced with permission from: **a**, ref. 82, © 1990 ACS; **b**, ref. 84, © 2008 IOP; **d**, ref. 39, © 1994 APS.

$\kappa_T$  rises anomalously. In fluids this derives from the reorganization of density fluctuations and in crystals from reconfiguration of nanodomains. Accordingly,  $B/G \rightarrow 0$  and therefore Poisson's ratio decreases. Figure 5a illustrates this for a volume transition in a polymer gel close to a critical point<sup>82</sup> and Fig. 5b for the  $\alpha$ - $\beta$  transition in crystalline quartz<sup>83,84</sup>. Similar behaviour is reported for different gel concentrations<sup>85</sup> and for different quartz grain sizes<sup>84</sup>, both of which affect the phase transition temperatures. In all cases the transitions are of first order, and accompanied by a very narrow minimum in  $\nu$ , mirroring the behaviour of the isothermal bulk modulus  $B$ . These substantial negative swings in  $\nu$  provide a distinctive universal signature for phase transitions, whatever the type of material. In mixed valence transitions in  $\text{YbInCu}_4$  (ref. 61), the cubic crystal structure does not change; but the bulk modulus softens and Poisson's ratio drops over a narrow range of temperature near 67 K. Softening of the bulk modulus also occurs for the ferroelastic cubic-tetragonal transition in  $\text{BaTiO}_3$ , in the vicinity of the Curie point, with an auxetic minimum in  $\nu$  (ref. 86).

Negative elastic moduli, for which Poisson's ratio falls outside the range  $-1$  to  $1/2$ , entail instability (Fig. 1b) which in some cases can be constrained. For transformations governed by stress-induced diffusion, the compressibility is predicted to diverge<sup>87</sup>, the bulk modulus softening to zero corresponding to a substantial lowering of  $\nu$ . But this is a slow process for which the relaxation time increases as the critical temperature is approached. For anisotropic single crystals such as  $\text{KH}_2\text{PO}_4$ , the shear elastic tensor element  $C_{66}$  softens to zero during phase transformation<sup>8</sup>. Softening of the shear or the bulk modulus of perovskite minerals<sup>11</sup> has been reported, and martensitic transformations are also characterized by a change in shear elastic moduli associated with changes in crystal structure. Poisson's ratios are typically not reported in such studies; in anisotropic solids they depend on multiple tensor elements. For the glass-to-rubber transition in polymers the shear modulus may change by more than a factor of a thousand, and the bulk modulus by about a factor of two<sup>18</sup>. As illustrated in Fig. 2e,  $\nu$  is about 0.3 in the glassy regime rising to nearly 0.5 in the rubbery regime<sup>20</sup>. Inorganic glasses exhibit similar behaviour above the glass transition  $T_g$ . The occurrence of flow indicates that the shear modulus tends to zero and Poisson's ratio to 0.5, as can be clearly seen for fragile melts in Fig. 4b.

**Shock-wave melting of metals** Despite its importance across the physical sciences, melting remains incompletely understood in terms of temperature-pressure melting curves and the underlying equations of state<sup>26</sup>. Nevertheless, significant experimental advances have been made in high-pressure/high-temperature physics where Poisson's ratio offers a unifying approach<sup>33-37,83,88</sup>. Figure 5c compiles data from the shock-wave melting of metals. The inner and outer pressure limits of the Earth's core surround the melting of Fe, underlining the relevance of these experiments for determining the temperature of the core by parameterizing the equations of state<sup>36</sup>. Melting metals at these extreme temperatures and pressures is clearly also relevant in developing new materials capable of withstanding extreme conditions.

Shock melting is accompanied by a sharp increase in Poisson's ratio to the liquid value of 0.5, pinpointed by the intersection of the shock adiabatic, or Hugoniot, with the melting curve obtained from the equations of state<sup>35</sup>. Despite the adiabatic nature, most of the melting thresholds are initiated by the small dip in  $\nu$  expected for first-order transitions. Melting is traditionally understood to occur as the average root-mean-square displacement of atoms in the solid state approaches  $\sim 10\%$  of the average interatomic separation—the so-called Lindemann criterion<sup>26</sup>. More specifically, melting coincides with the momentary rise in  $\kappa$ , the onset of intersite diffusion and  $G \rightarrow 0$ . All these related components, both before melting and on melting, contribute to the striking melting signature in Poisson's ratio (Fig. 5c).

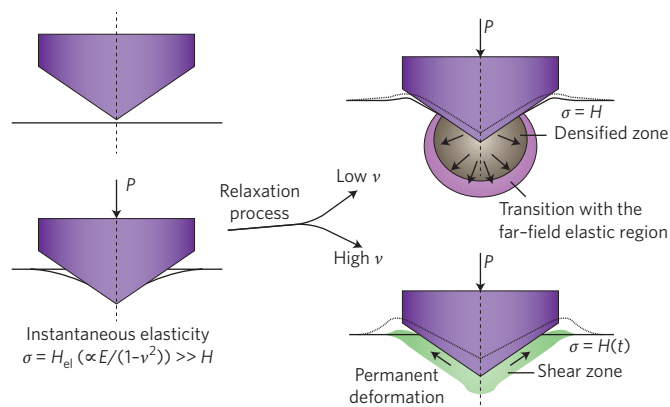


**Figure 6 | Indentation of glasses: densification or shear flow.** The effects of  $\nu$  are seen in the stages of deformation under indentation. The surface profiles are shown for the indenter at maximum load (solid lines) and after unloading (dotted lines). Arrows indicate matter displacement.  $\sigma$  is the mean contact pressure. Reproduced with permission from ref. 46, © 2010 AIP.

Another interesting observation from Fig. 5c is the same crystalline metallic phase generally persisting up to  $T_m$ . For molybdenum, though, melting is anticipated by an intermediate phase transition near 150 GPa. Originally interpreted as a bcc to hcp transition<sup>35</sup>, recent X-ray measurements of the melting curve for Mo, made in a diamond-anvil cell, suggest that values of Poisson's ratio before  $T_m$ , which are unusually high for bcc metals (Fig. 1c), point to a new intermediate non-crystalline phase<sup>34</sup>—perhaps a low-density polymorph. Also included in Fig. 5c are the brittle-ductile  $\nu$  thresholds taken from Fig. 7c, Mo for example melting from the plastic region, with Fe on the borderline.

**Polyamorphic phases in tetrahedral glasses** Polyamorphism occurs when amorphous phases in the same liquid or supercooled state share the same composition, but differ in density and entropy<sup>79,89</sup>. The HDA phase generally has higher entropy than the LDA phase<sup>89</sup>, in which case the slope of the phase boundary  $dT/dP = dV/dS < 0$ . Polyamorphism is not in dispute, but whether or not transformations between polyamorphic phases are of first order is controversial<sup>38,58,59,79,80,89,90</sup>. In addition to LDA and HDA amorphous ice<sup>58,59</sup>, polyamorphism has been reported in many tetrahedral glasses<sup>89</sup>. For silica under pressure Si-O polyhedra change from tetrahedral coordination eventually to octahedral coordination<sup>91</sup> reminiscent of the high-density  $\text{SiO}_2$  crystalline phase stishovite. For both HDA ice<sup>58</sup> and densified silica<sup>39</sup>, careful *in situ* sound velocity experiments reveal major changes in elastic moduli at these phase transformations. Values of Poisson's ratio are shown in Fig. 5d for silica<sup>39</sup>. Starting from low values of  $\nu$  indicative of an LDA phase, densification results in a significant rise in  $\nu$  as the HDA phase is formed, but this is preceded by a downward dip, indicative of a first-order transition. Decompression returns a densified tetrahedral phase<sup>39</sup>.

Since these discoveries, a wealth of new densified HDA phases obtained from crystalline precursors have been reported<sup>79,92</sup>. Creating LDA phases by this route initially proved more challenging, as decompression without cavitation is difficult to achieve in condensed matter. An alternative approach has been discovered that involves the amorphization of microporous crystalline materials, such as zeolites<sup>38,93-95</sup>, tungstates<sup>96</sup> or metal-organic frameworks<sup>97</sup>. Notwithstanding the considerable directional swings exhibited by single crystals<sup>25,74</sup>, Poisson's ratio for these low-density crystalline materials typically averages out around 0.2. Amorphization occurs at pressures of a few gigapascals<sup>93-96</sup> at ambient temperature and close to  $T_g$  at ambient pressure<sup>93,97</sup>. *In situ* small-angle X-ray scattering

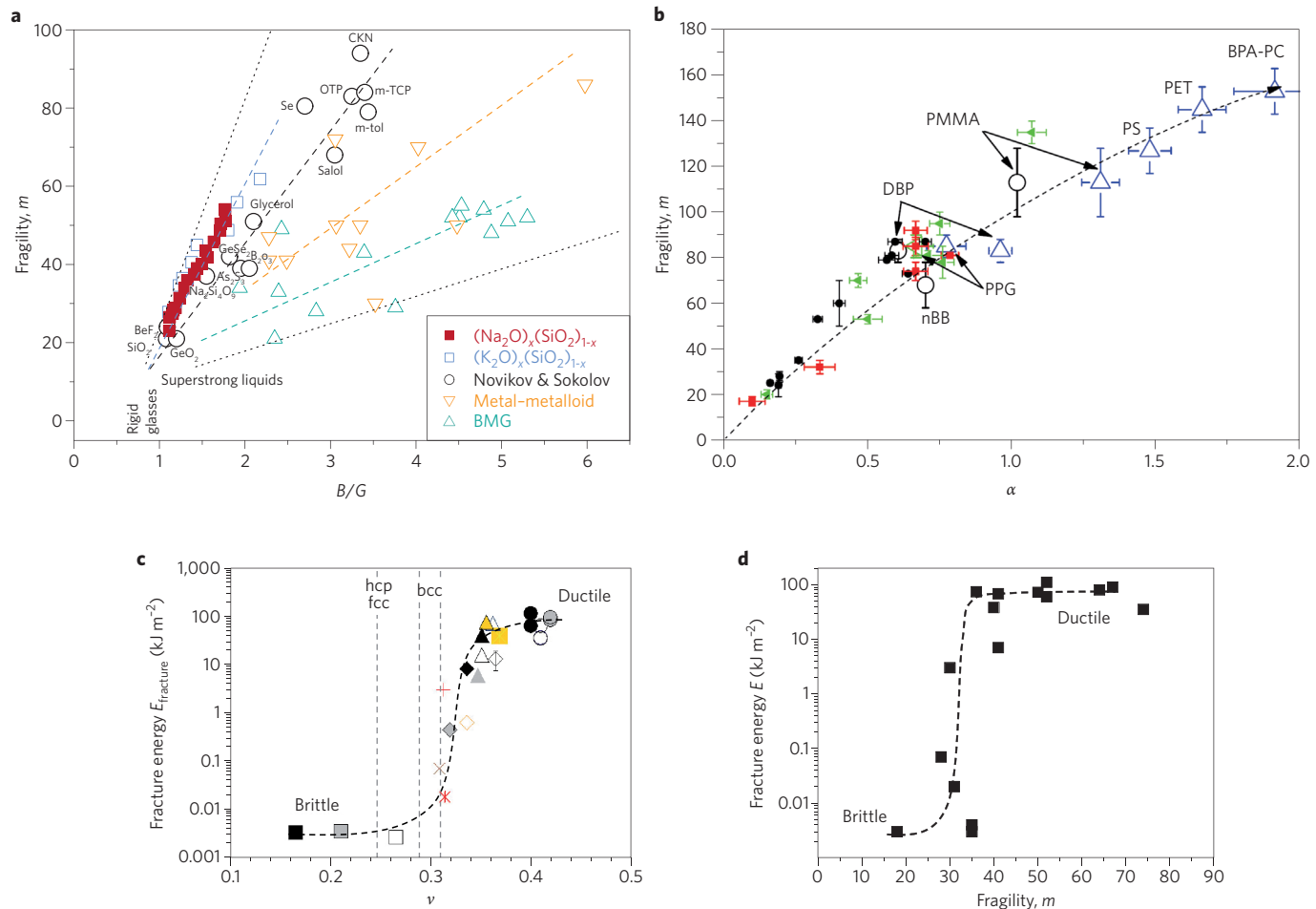


**Figure 7 | Poisson's ratio, non-ergodicity and fracture toughness.** **a**, Novikov-Sokolov plot<sup>100</sup> of melt fragility  $m$  versus  $B/G$  for single-phase glass-formers, with modified glasses and metallic glasses added<sup>79,102,112</sup>, showing an increase in the slope of  $m$  versus  $B/G$  with atomic packing, the different families converging on superstrong melts and perfect glasses. **b**, Scopigno plot<sup>105</sup> of melt fragility  $m$  versus  $\alpha$  for an extended range of inorganic and organic glass-formers<sup>106</sup>, where  $\alpha = (1 - f_0)T_g/T$  and  $f_0$  is the non-ergodicity factor that measures the departure from thermodynamic equilibrium (Box 2). **c**, Fracture energy  $\log E_{\text{fracture}}$  versus  $\nu$  for bulk metallic glasses<sup>30</sup> showing an abrupt brittle-ductile threshold for  $\nu \approx 0.31$ . Thresholds for polycrystalline metals are indicated by vertical lines<sup>30</sup>. **d**, Fracture toughness  $\log E_{\text{fracture}}$  versus  $m$  for bulk metallic glasses, differentiating ductile from brittle character, with a sharp threshold close to  $m \approx 30$ . Dashed curves in **c** and **d** are included to guide the eye. Figure reproduced with permission from: **a**, ref. 79, © 2007 Taylor & Francis; **b**, ref. 106, © 2010 APS; **c**, ref. 50, © 2005 Taylor & Francis.

(SAXS)<sup>93</sup> and inelastic X-ray scattering experiments<sup>38,98</sup> reveal that Poisson's ratio drops considerably during amorphization before the final HDA glass is formed, by which time  $\nu$  is close to 0.25, similar to other aluminosilicate glasses<sup>42</sup>. The contrasting morphology, between microporous crystals and the HDA glass shown in the side panels of Fig. 8a, reveals evidence of flow at  $T_g$ . Interestingly, this is an exothermic process<sup>93</sup> during which the SAXS intensity  $I_{\text{SAXS}}$  rises and falls by an order of magnitude<sup>93</sup>. As  $I_{\text{SAXS}}$  is in turn proportional to the isothermal compressibility  $\kappa_T$  (ref. 79) the  $I_{\text{SAXS}}$  peak points to a substantial minimum in  $B$ , and therefore in  $\nu$ , consistent with the first-order phase transitions illustrated in Fig. 5a and b. Such an order-order displacive transition from a microporous crystal has been verified by atomistic simulation during the densification of zeolite A<sup>99</sup>. Atomistic models of the low-entropy LDA or 'perfect glasses'<sup>79</sup> formed from other microporous crystalline materials have been reported<sup>95-97</sup>. Poisson's ratios for these ordered glasses are expected to be significantly smaller than their melt-quenched HDA counterparts<sup>38</sup>.

**Low-frequency collective modes and the boson peak** The driving force for polyamorphic transitions in microporous zeolites seems to lie in the strong phonon band found at low frequencies at the start

of the vibrational density of states (VDOS), preceded by a narrow band related to the rotation of connected tetrahedra (Fig. 8a and Box 2)<sup>94</sup>. In glasses this feature in the VDOS is generically referred to as the boson peak (because it generally scales with the Bose-Einstein function), and its origin has been fiercely argued over for the past two decades<sup>79</sup>. During microporous collapse, however, a strong correlation exists between the intensity and frequency of terahertz vibrations and the material density  $\rho$  (ref. 94) which can be attributed to librational driven resonances of zeolitic subunits and which decrease as the HDA glass is formed (Fig. 8a). This densification behaviour of the low-frequency VDOS is reflected more generally across the whole of the glassy state<sup>79,91,100</sup>, the frequency  $\omega_{\text{BP}}$  increasing and the size  $A_{\text{BP}}$  decreasing with increasing  $\rho$ . Densified silica provides a good example<sup>91</sup>. Indeed, a universal curve can usually be obtained by normalizing to  $\omega_{\text{BP}}$  and  $A_{\text{BP}}$ .

There is a lot of experimental evidence that the boson peak in the glassy state has transverse character, with a suspicion that its frequency  $\omega_{\text{BP}}$  may be linked to the Ioffe-Regel limit, where the mean free path of phonons approaches their wavelength and beyond which they no longer propagate<sup>79,101-103</sup>. Strong confirmation for this view has come from the simulations shown in Fig. 8b which replicate experimental findings. Moreover,  $\omega_{\text{BP}}$  equates with the

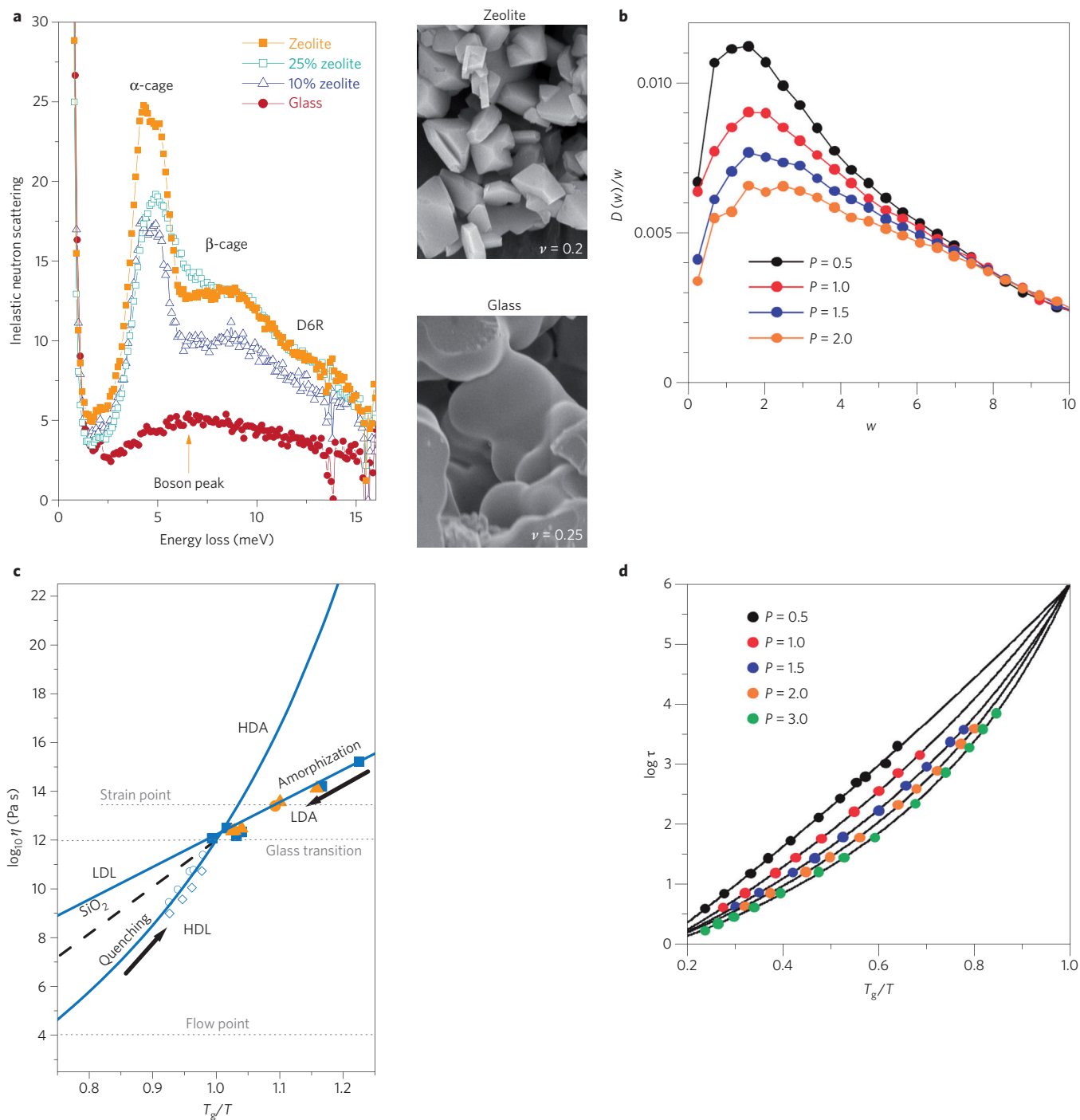


**Figure 8 | Boson peak and melt fragility.** **a**, Reduction in low-frequency collective terahertz band during the collapse of zeolite Y with densification<sup>94</sup> (left) ending in the formation of a glass. Zeolitic subunits  $\alpha$  and  $\beta$  cages and double six-fold rings (D6R) features are retained in the LDA phase, even when 90% of the zeolite has amorphized. Reproduced with permission from ref. 94, © 2005 AAAS. Micrographs of zeolite and final glass (right) reveal onset of viscous flow as part of the LDL–HDL transition. Reproduced from ref. 93, © 2003 NPG. **b**, Reduction in the size of the boson peak ABP =  $D(\omega)/\omega$  calculated for a 2D glass-forming system under increasing pressure  $P$ , where  $D(\omega)$  is the VDOS for acoustic modes<sup>103</sup>. **c**, Temperature dependence of the viscosity  $\eta$  versus  $T_g/T$  of the HDL and LDL supercooled phases together with the HDA and LDA glasses associated with the collapse of zeolite A. This shows how the increase in melt fragility  $m$  follows the LDA–HDA increase in densification<sup>93</sup>. The classical strong liquid  $\text{SiO}_2$ , whose fragility falls between those of the two liquid phases, is included for comparison. **d**, Temperature dependence ( $T_g/T$ ) of the structural relaxation time  $\tau$  calculated for the 2D glass in **b**, showing the increase in melt fragility with increasing pressure  $P$  (ref. 103). Note that the fragility is given by  $m = [\partial \log \eta(T)/(\partial T_g/T)]_{T=T_g}$  and that  $\eta$  and  $\tau$  are related by  $\eta = G_\infty \tau_\alpha$  (Box 2). Figure reproduced or adapted from: **b,d**, ref. 103, © 2008 NPG; **c**, ref. 93, © 2003 NPG.

exciting frequency  $\omega_{\text{IR}}^{\text{T}}$  at the Ioffe–Regel limit for transverse waves, compared with the exciting frequency for longitudinal waves  $\omega_{\text{IR}}^{\text{L}}$  which far exceeds  $\omega_{\text{BP}}$ . In a similar way,  $A_{\text{BP}}$  scales with the VDOS for transverse phonons as the structure is densified. As  $A_{\text{BP}}$  decreases,

$\nu$  should increase<sup>101</sup> with decreasing  $G$  (Box 2) and, beyond the plastic limit, plastic flow should occur (Fig. 6). Conversely, if the collective dynamics of connected polyhedra are significant,  $\nu$  will be reduced with increased  $G$  encouraging embrittlement beyond the

elastic limit<sup>31,51</sup>. Indeed, Poisson's ratio provides a sharp criterion for differentiating brittleness from ductility in crystalline<sup>30,31</sup> and in amorphous<sup>50,51</sup> metals (see Fig. 7c). A more controversial relationship is between  $\nu$  and the fragility  $m$  of the corresponding supercooled liquid<sup>100–102,104</sup> (Fig. 7a). Together with the degree of non-ergodicity  $f_0$  frozen into the glass<sup>79,105,106</sup>, the melt fragility  $m$  is measured at the glass transition  $T_g$  (Box 2) where the viscous relaxation time reaches  $\sim 100$  s and the liquid is considered solid<sup>26,79,107–109</sup>. Its elastic properties, however, clearly differ from those measured under ambient conditions (Fig. 4b). How, then, can the dynamics of the liquid state be related to the elastic properties of the solid state? Indeed, how do solids melt?

### Melt fragility and solid elastic properties

**Melt fragility** The hugely different viscous properties of liquids are illustrated in the familiar Angell plot of  $\log \eta$  versus  $T_g/T$ , where  $\eta$  is shear viscosity, shown in Box 2 (ref. 108). In particular, liquid fragility is defined by the steepness of shear viscosity  $\eta$  as a function of reciprocal temperature as  $T_g$  is approached<sup>79,107–109</sup>, differentiating 'strong' liquids such as silica from 'fragile' liquids like molecular melts. The structural relaxation time  $\tau$  of the liquid is directly related to  $\eta$ , so strong melts rheologically approach  $T_g$  much more gradually than fragile melts (Box 2). This distinction is even greater at the melting temperature  $T_m$  where solid and liquid coexist but where liquid structural relaxation times can differ by as much as  $10^6$ . Accordingly solids—crystals or glasses—forming strong liquids melt or soften far more slowly than those forming fragile liquids: that is, these transformations are much more viscoelastic (Fig. 2e), as can be seen, for example, in  $\nu$  versus  $T/T_g$  curves (Fig. 4b) by the very different rates at which Poisson's ratio approaches 0.5 when glasses soften.

With densification, supercooled liquids become more fragile. The increase in fragility can be seen in Fig. 8c for the LDA–HDA transitions underpinning the collapse of a low-density zeolite<sup>93</sup>; the viscosity of the corresponding fragile HDL liquid meets the glass transition  $T_g$  from above far more steeply than the viscosity of the LDA phase from below  $T_g$ . Atomistic simulations for a 2D glass-forming system<sup>103</sup> reveal similar behaviour, with  $m$  increasing with increasing pressure (Fig. 8d). Comparing densification changes in  $m$  (Fig. 8c and 8d) with the magnitude of the terahertz peak in the glassy state (Fig. 8a and 8b), it is clear that these are inversely related. Strong liquids form glasses with many more collective modes than do fragile liquids. Strong liquids, too, are good glass formers, whereas fragile liquids are prone to crystallize. Glass formation and crystallization are competitive kinetic processes, with collective modes favouring the former.

**Poisson's ratio and non-ergodicity** Covering a broad range of single-phase glasses, two interesting empirical relationships have emerged linking melt fragility with the elastic properties of the glass<sup>100–102,105,106</sup>,  $m$  versus  $B/G$  and  $m$  versus  $\alpha$ . The ratio  $B/G$  relates directly to Poisson's ratio  $\nu$  and  $\alpha$  to the non-ergodicity factor  $f_0$  (ref. 79; Box 2), which describes the extent of the departure from thermodynamic equilibrium. The plot of  $m$  versus  $B/G$  (Fig. 7a) reveals how Poisson's ratio  $\nu$  increases across many glasses, as the melts from which they are quenched increase in fragility  $m$  (refs 100–102). Although objections to this relationship were originally voiced<sup>104,110</sup>, many of these have been overcome as more glasses have been added<sup>79,101,102,106,111,112</sup> and the central proposition that "the fragility of a liquid (might be) embedded in the properties of its glass"<sup>91,105</sup> has generally been strengthened. Although it is true that the point scatter in the  $m$  versus  $B/G$  plots is considerable, it is also clear that groups of glasses can be differentiated<sup>79,111</sup>, forming an approximately radial arrangement from modified oxide glasses through single glass formers to the dense metallic glasses. The overall distribution narrows towards the glasses associated with the strongest liquids<sup>38,79</sup>. Although silica is usually considered the

strongest of these, experiments on zeolite amorphisation reveal that for new low-density liquids (LDL)  $m \leq 10$  (ref. 93; Fig. 8c), with the associated LDA glasses being topologically ordered<sup>38,79,99</sup>. The  $m$  versus  $\alpha$  plot<sup>105,106</sup> (Fig. 7b) shows that when liquid fragility  $m$  increases, glasses become more ergodic, with  $f_0$  (Box 2) decreasing. Specifically,  $f_0$  equates with the autocorrelation function of the liquid density fluctuations over the longest timescales<sup>79,107,109</sup>. It is readily obtained from inelastic X-ray scattering experiments at different temperatures<sup>113</sup>, measuring the extent to which density fluctuations in the melt are captured in the structure of the glass<sup>105,109</sup>.

From the empirical relationships  $m$  versus  $B/G$  and  $m$  versus  $\alpha$  it is clear that  $\nu$  and  $\alpha$  must also be interrelated across families of glasses, meaning that the least ergodic glasses (small  $\alpha$ ) are the most distortable (small  $\nu$ ) and vice versa. This important conclusion can be better understood by recognizing that the non-ergodicity of a glass is related to the ratio of the sound velocities  $V_t/V_l$  (ref. 100), which in turn records the density fluctuations in the glass (Box 2). These ripples in the nanostructure are considered to be related in turn to the size of the boson peak  $A_{BP}$  (refs 100,101,109). If  $\alpha \propto B_{\infty}/G_{\infty}$ , then glasses with the strongest boson peak should have the largest non-ergodicity ( $f_0$  at  $T_g$ ) and therefore the smallest  $\alpha$ . As  $\alpha$  correlates with  $m$  (refs 105,106), their associated melt fragilities will also be the lowest (Fig. 7b), as will their Poisson's ratio (Fig. 7a), their shear resistance and, beyond the yield point, their tendency to crack (Fig. 7c): strong liquids form brittle glasses slowly, fragile liquids ductile glasses rapidly.

The original relationship<sup>105</sup> between  $m$  and  $\alpha$  has recently been systematically developed to account for the presence of secondary relaxation processes<sup>106</sup>. These are particularly prevalent in polymers and their associated liquids which are very fragile. Figure 7b shows the correlation extending over more than twice the previous range<sup>105</sup>, further strengthening the evidence that the correlation between melt fragility and vibrational properties of the corresponding amorphous solid is a universal feature of glass formation.

### Brittle–ductile transformation

Ductility and brittleness relate to the extreme response of materials strained outside their elastic limits, so any relationship with  $\nu$  would seem at first non-intuitive. However, Poisson's ratio measures the resistance of a material to volume change ( $B$ ) balanced against the resistance to shape change ( $G$ ). Occurring within the elastic regime, any links with properties beyond the yield point must necessarily involve the time-dependent processes of densification and/or flow, already discussed for glasses above. Just as viscoelastic behaviour is expressed in terms of time-dependent bulk and shear moduli, with Poisson's ratio  $\nu(t)$  gradually changing between elastic values, we might expect the starting value of  $\nu$  to provide a metric for anticipating mechanical changes, not just in glasses but also in crystalline materials, resulting in ductility (starting from a high  $\nu$ ) or embrittlement (starting from a low  $\nu$ ). At either extreme the microstructure will play a part, whether through cracks, dislocations, shear bands, impurities, inclusions or other means<sup>114</sup>.

**Polycrystalline materials** Polycrystalline materials, in the idealized case where there is no preferred orientation, are macroscopically isotropic. Unlike glasses which are generally homogeneous and isotropic but lack atomic long-range order<sup>79,107,109</sup>, polycrystalline materials have unit cell symmetry but atomic periodicity is broken internally by dislocations and impurities, and externally by grain boundaries<sup>30,31</sup>. Although there is no simple link between interatomic potentials and mechanical toughness in polycrystalline materials, Poisson's ratio  $\nu$  has proved valuable for many years as a criterion for the brittle–ductile transition exhibited by metals<sup>30,31,32,115</sup>, just as it is now helping to distinguish brittle glasses from ductile glasses (Fig. 7c) which, from Fig. 7a, are associated with strong and fragile melts respectively<sup>79,100,101</sup>.

The old proposal that grains in polycrystalline materials might be cemented together by a thin layer of amorphous material ‘analogous to the condition of a greatly undercooled liquid’<sup>116</sup> has often been challenged. However, recent atomistic simulations of crystalline grains and grain boundaries seem to confirm the dynamic consequences of this idea in many details<sup>117</sup>. The strengths of pure metals at low temperatures are known to be mainly governed by the strengths of grain boundaries<sup>30</sup>. These usually exceed the crystalline cleavage strength, which is governed by the dynamics of dislocations generated at the crack tip<sup>31</sup>. The correlation between  $m$  and  $B/G$  in glasses (Fig. 7a) suggests that the mechanical toughness of metals might also be related to the fragility of the undercooled melt from which they are cast and from which the grain boundaries seem to be quenched. This would suggest that soft metals like gold, silver or copper might be ductile because they originate from melts that are fragile. Conversely, hard metals such as tungsten, iridium or chromium might be brittle because, as melts, they are stronger. If this were the case then there would be consequences for the density fluctuations frozen into the grain boundaries, which will be weaker for soft metals than for brittle metals. By the same token, grain boundaries would be more ergodic in soft compared with brittle metals.

**Metallic glasses** Because direct experimental evidence is lacking, linking melt fragility and mechanical toughness for polycrystalline metals can only be speculative. In metallic glasses, though—particularly bulk metallic glasses (BMG) that are cast by slow cooling like conventional glasses<sup>118</sup>—sufficient data on elastic moduli and toughness<sup>50</sup> are available, as well as on melt fragility<sup>102</sup>, to test these ideas quantitatively. In the first place the threshold between brittleness and ductility in metallic glasses is very abrupt (Fig. 7c). From the most brittle metallic glasses to the toughest, fracture energies  $E_{\text{fracture}}$  increase by as much as four decades<sup>50</sup>. The brittle–ductile threshold occurs close to  $B/G \approx 2.4$  ( $\nu = 0.32$ ) and is generally higher than the thresholds reported for polycrystalline metals<sup>30,31</sup> (Fig. 7c). It is also more sharply defined than for crystalline metals. Plastic flow in metallic glasses occurs very locally in shear bands<sup>51,114</sup>, compared with polycrystalline metals where flow is dislocation-mediated, and delocalized by associated work-hardening<sup>30</sup>.

Turning now to the BMG melt fragilities,  $m$  rises with  $B/G$ , but not as steeply as for network and molecular liquids and their glasses (Fig. 7a). Comparing this with  $\log E_{\text{fracture}}$  versus  $\nu$  (Fig. 7c) points to the cross-correlation between fracture energy and melt fragility,  $\log E_{\text{fracture}}$  versus  $m$ , plotted in Fig. 7d. This is very sharp, clearly showing how brittle BMGs (low  $E_{\text{fracture}}$ , low  $\nu$ ) correlate with strong melts (low  $m$ ) and ductile BMGs (high  $E_{\text{fracture}}$ , high  $\nu$ ) with fragile melts (high  $m$ ), as we have suggested might be the case for grain boundaries in crystalline metals.

The elegant work of Jiang and Dai<sup>32</sup> (Fig. 1c) explores relations between elastic moduli in crystalline and glassy metals in terms of a Milton map<sup>11</sup>. Earlier these authors reported an intrinsic correlation between the bulk modulus for a wide range of metallic glasses and the fragilities of the liquids from which they are cast<sup>102</sup>. The dashed lines in Fig. 1c correspond to brittle–ductile Poisson’s ratio thresholds, suggesting a common phenomenology. Recalling that fracture energy and melt fragility are correlated (Fig. 7d), it seems likely that the ductile and brittle properties of metals, whether they are glasses or crystals, are intimately related to the viscous time-dependent properties of their supercooled antecedents, either constrained in metallic glass shear bands<sup>51</sup> or, more speculatively, in polycrystalline grain boundaries<sup>117</sup>.

### Future perspectives

Scientists from many different fields still ignore the variability of Poisson’s ratio. In finite-element simulation for instance, calculation in the elastic or ductile regimes usually assumes that  $\nu$  is fixed and  $\sim 0.3$ . In physics,  $\nu$  is often assumed to have little effect on the

vibrational density of states, although it shows up explicitly in the Debye equation. Therefore, we hope that this Review on Poisson’s ratio will encourage researchers and engineers to pay more attention to this index, which is directly relevant to modern materials. Auxetic behaviour is an obvious example, as is the distinctive signature of Poisson’s ratio for phase transitions, including melting. Conversely, the dynamics of the liquid state are contributing to our understanding of the elastic properties of the glassy state via Poisson’s ratio and, in turn, the distinction between the brittleness and ductility of materials. For the future, the numerical metric that Poisson’s ratio provides will be advantageous in researching and developing new materials, marrying the mechanical response of diverse components, from the nano- to the macroscale through variable changes in shape and volume.

### References

1. <http://gallica.bnf.fr/>.
2. Poisson, S. D. *Traité de Mécanique* 2, 476 (1811).
3. Poisson, S. D. *Ann. Chim. Phys.* (eds Gay-Lussac, L. J. & Arago, F.) **36**, 384–385 (1827).
4. Cauchy, A. L. Sur les équations qui expriment les conditions d’équilibre, ou les lois du mouvement intérieur d’un corps solide élastique ou non élastique. *Exercices de Mathématiques* vol. 3 (1828).
5. Voigt, W. Allgemeine Formeln für die Bestimmung der Elasticitätsconstanten von Krystallen durch die Beobachtung der Biegung und Drillung von Prismen. *Ann. Phys.* **16**, 273–310; 398–415 (1882).
6. Love, A. E. H. *A Treatise on the Mathematical Theory of Elasticity* (Dover, 1944).
7. Haeri, A. Y., Weidner, D. J. & Parise, J. B. Elasticity of  $\alpha$ -cristobalite: a silicon dioxide with a negative Poisson’s ratio. *Science* **257**, 650–652 (1992).
8. Evans, K. E., Nkansah, M. A., Hutchinson, I. J. & Rogers, S. C. Molecular network design. *Nature* **353**, 124, (1991). This paper introduces the term auxetic, from the root word for growth, to describe expansion under tension.
9. Lakes, R. S. Foam structures with a negative Poisson’s ratio. *Science* **235**, 1038–1040 (1987).
10. Caddock, B. D. & Evans, K. E. Microporous materials with negative Poisson’s ratios. I: Microstructure and mechanical properties. *J. Phys. D.* **22**, 1877–1882 (1989).
11. Milton, G. Composite materials with Poisson’s ratios close to  $-1$ . *J. Mech. Phys. Solids* **40**, 1105–1137 (1992).
12. Lakes, R. S. Advances in negative Poisson’s ratio materials. *Adv. Mater.* **5**, 293–296 (1993).
13. Alderson, K. L. & Evans, K. E. The fabrication of microporous polyethylene having negative Poisson’s ratio. *Polymer*, **33**, 4435–4438 (1992).
14. Baughman, R. H., Shacklette, J.-M., Zakhidov, A. A. & Stafström, S. Negative Poisson’s ratio as a common feature of cubic metals. *Nature* **392**, 362–365 (1998).
15. Sanchez-Valle, C. *et al.* Negative Poisson’s ratios in siliceous zeolite MFI-silicalite. *J. Chem. Phys.* **128**, 184503 (2008).
16. Hall, L. J. *et al.* Sign change of Poisson’s ratio for carbon nanotube sheets. *Science* **320**, 504–507 (2008).
17. Smith, C. W., Wootton, R. J. & Evans, K. E. Interpretation of experimental data for Poisson’s ratio of highly nonlinear materials. *Exp. Mech.* **39**, 356–362 (1999).
18. Tschoegl, N. W., Knauss, W. J. & Emri, I. Poisson’s ratio in linear viscoelasticity, a critical review. *Mech. Time-Depend. Mater.* **6**, 3–51 (2002).
19. Lakes, R. S. & Wineman, A. On Poisson’s ratio in linearly viscoelastic solids. *J. Elast.* **85**, 46–63 (2006).
20. Lu, H., Zhang, X. & Krauss, W. G. Uniaxial, shear, and Poisson relaxation and their conversion to bulk relaxation: studies on poly(methyl methacrylate). *Polym. Eng. Sci.* **37**, 1053–1064 (1997).
21. <http://www.youtube.com/watch?v=BN2D5y-AxIY>.
22. Wang, Y. C. & Lakes, R. S. Composites with inclusions of negative bulk modulus: extreme damping and negative Poisson’s ratio. *J. Comp. Mater.* **39**, 1645–1657 (2005).
23. Smith, C. W., Grima, J. N. & Evans, K. E., A novel mechanism for generating auxetic behaviour in reticulated foams: missing rib foam model. *Acta Mater.* **48**, 4349–4356 (2000).
24. Baughman, R. H. *et al.* Negative Poisson’s ratios for extreme states of matter. *Science* **288**, 2018–2022 (2000).
25. Grima, J. N., Jackson, R., Alderson, A. & Evans, K. E. Do zeolites have negative Poisson’s ratios? *Adv. Mater. B* **12**, 1912–1918 (2000).
26. Poirier, J.-P. *Introduction to the Physics of the Earth’s Interior* (Cambridge Univ. Press, 2000).
27. Cohen, M. L. Calculation of bulk moduli of diamond and zinc-blende solids. *Phys. Rev. B* **32**, 7988–7991 (1985).

28. Fukumoto, A. First-principles pseudopotential calculations of the elastic properties of diamond, Si, and Ge. *Phys. Rev. B* **42**, 7462–7469 (1990).
29. Perottoni, C. A. & Da Jornada, J. A. H. First-principles calculation of the structure and elastic properties of a 3D-polymerized fullerite. *Phys. Rev. B* **65**, 224208 (2002).
30. Cottrell, A. H. in *Advances in Physical Metallurgy* (eds Charles, J. A. & Smith, G. C.) (Inst. Metals, London, 1990).
31. Kelly, A., Tyson, W. R. & Cottrell, A. H. Ductile and brittle crystals. *Phil. Mag.* **15**, 567–586 (1967).
32. Jiang, M. Q. & Dai, L. H. Short-range-order effects on the intrinsic plasticity of metallic glasses. *Phil. Mag. Lett.* **90**, 269–277 (2010).
33. McQueen, R. G., Hopson, J. W. & Fritz, J. N. Optical technique for determining rarefaction wave velocities at very high pressures. *Rev. Sci. Instrum.* **53**, 245–250 (1982).
34. Santamaría-Pérez, D. *et al.* X-ray diffraction measurements of Mo melting at 119 GPa and the high pressure phase diagram. *J. Chem. Phys.* **130**, 124509 (2009).
35. Hixson, R. S., Boness, D. A. & Shaner, J. W., Acoustic velocities and phase transitions in molybdenum under strong shock compression. *Phys. Rev. Lett.* **62**, 637–640 (1989).
36. Nguyen, J. H. & Holmes, N. C. Melting of iron at the physical conditions of the Earth's core. *Nature* **427**, 339–342 (2004).
37. Jensen, B. J., Cherne, E. J. & Cooley, J. C. Shock melting of cerium. *Phys. Rev. B* **81**, 214109 (2010).
38. Greaves, G. N. *et al.* Zeolite collapse and polymorphism. *J. Phys. Cond. Mat.* **19**, 415102 (2007).
39. Zha, C.-S., Hemley, R. J., Mao, H.-K., Duffy, T. S. & Meade, C. Acoustic velocities and refractive index of SiO<sub>2</sub> glass to 57.5 GPa by Brillouin scattering. *Phys. Rev. B* **50**, 13105–13112 (1994).
40. Zeng, Z.-Y., Hu, C.-E., Cai L.-C., Chen, X.-R. & Jing, F.-Q. Lattice dynamics and thermodynamics of molybdenum from first-principles calculations. *J. Phys. Chem. B* **114**, 298–310 (2010).
41. Davies, R. A. *et al.* Geometric, electronic and elastic properties of dental silver amalgam  $\gamma$ -(Ag<sub>2</sub>Sn),  $\gamma_1$ -(Ag<sub>2</sub>Hg<sub>3</sub>),  $\gamma_2$ -(Sn<sub>8</sub>Hg) phases, comparison of experiment and theory. *Intermetallics* **18**, 756–760 (2010).
42. Rouxel, T. Elastic properties and short-to-medium range order in glasses. *J. Am. Ceram. Soc.* **90**, 3019–3039 (2007).
43. Makishima, A. & Mackenzie, J. D. Calculation of bulk modulus, shear modulus and Poisson's ratio of glass. *J. Non-Cryst. Sol.* **17**, 147–157 (1975).
44. Antao, S. M. *et al.* Network rigidity in GeSe<sub>2</sub> glass at high pressure. *Phys. Rev. Lett.* **100**, 115501 (2008).
45. Nicholas, J., Sinogeikin, S., Kieffer, J. & Bass J. A high pressure Brillouin scattering study of vitreous boron oxide up to 57 GPa. *J. Non-Cryst. Sol.* **349**, 30–34 (2004).
46. Rouxel, T., Ji, H., Guin, J. P., Augereau, F. & Rufflé, B. Indentation deformation mechanism in glass: densification versus shear flow. *J. Appl. Phys.* **107**, 094903 (2010).
47. Rouxel, T., Ji, H., Hammouda, T. & Moreac, A. Poisson's ratio and the densification of glass under high pressure. *Phys. Rev. Lett.* **100**, 225501 (2008).
48. Das, B. M. *Advanced Soil Mechanics* 2nd edn (Spon, 2002).
49. Ji, H., Robin, E. & Rouxel, T. Physics and mechanics of the deformation of plasticine: macroscopic indentation behaviour for temperature between 103–293 K. *J. Mech. Mat.* **41**, 199–209 (2009).
50. Lewandowski, J. J., Wang, W. H. & Greer, A. L. Intrinsic plasticity or brittleness of metallic glasses. *Phil. Mag. Lett.* **85**, 77–87 (2005).
51. Lewandowski, J. J. & Greer, A. L., Temperature rise at shear bands in metallic glasses. *Nature Mater.* **5**, 15–18 (2006).
52. Bridge, B. & Higazy, A. A. A model of the compositional dependence of the elastic moduli of multicomponent oxide glasses. *Phys. Chem. Glasses* **27**, 1–14 (1986).
53. Sreeram, A. N., Varshneya, A. K. & Swiler, D. R. Molar volume and elastic properties of multicomponent chalcogenide glasses. *J. Non-Cryst. Sol.* **128**, 294–309 (1991).
54. Moysan, C., Riedel, R., Harshe, R., Rouxel, T. & Augereau, F. Mechanical characterization of a polysiloxane-derived SiOC glass. *J. Europ. Ceram. Soc.* **27** 397–403 (2007).
55. Miracle, D. B. A structural model for metallic glasses. *Nature Mater.* **3**, 697–701 (2004).
56. Sheng, H. W., Luo, W. K., Alamgir, F. M., Bai, J. M. & Ma, E. Atomic packing density and short-to-medium range order in metallic glasses. *Nature* **439**, 419–425 (2006).
57. Hessinger, J., White, B. E. & Pohl, R. O. Elastic properties of amorphous and crystalline ice films. *Planet. Space Sci.* **44**, 937–944 (1996).
58. Loerting, T. & Giovambattista, N., Amorphous ices: experiments and numerical simulations. *J. Phys. Cond. Mat.* **18**, R919–R977 (2006).
59. Mishima, O., Calvert, L. D. & Whalley, E. 'Melting ice' I at 77 K and 10 kbar: a new method of making amorphous materials. *Nature* **310**, 393–395 (1984).
60. Gibson, L. J. & Ashby, M. F. *Cellular Solids* 2nd edn (Cambridge Univ. Press, 1997).
61. Beer, F. P. & Johnston, E. R. *Mechanics of Materials* (McGraw Hill, 1981); 2nd edn (1992).
62. Lakes, R. S. Negative Poisson's ratio materials. *Science* **238**, 551 (1987).
63. Wojciechowski, K. W. Two-dimensional isotropic system with a negative Poisson ratio. *Phys. Lett. A* **137**, 60–64 (1989).
64. Grima, J. N., Alderson, A. & Evans, K. E. Auxetic behaviour from rotating rigid units. *Phys. Stat. Solidi B* **242**, 561–75 (2005).
65. Rothenburg, L., Berlin, A. A. & Bathurst, R. J. Microstructure of isotropic materials with negative Poisson's ratio. *Nature* **354**, 470–472 (1991).
66. Silva, S. P. *et al.* Cork: properties, capabilities and applications. *Int. Mater. Rev.* **50**, 345–365 (2005).
67. Grima, J. N. *et al.* Hexagonal honeycombs with zero Poisson's ratios and enhanced stiffness. *Adv. Eng. Mater.* **12**, 855–862 (2010).
68. Barré de Saint-Venant, *Resumé des Leçons sur l'application de la mécanique à l'établissement des constructions et des machines*. Première section. De la Résistance des corps solides par Navier. 3ème édition avec des notes et des Appendices (Paris, 1848).
69. Lempriere, B. M. Poisson's ratio in orthotropic materials. *AIAA J.* **6**, 2226–2227 (1968).
70. Gunton, D. J. & Saunders, G. A. The Young's modulus and Poisson's ratio of arsenic, antimony, and bismuth. *J. Mater. Sci.* **7**, 1061–1068 (1972).
71. Kimizuka, H., Kaburaki, H. & Kogure, Y. Mechanism for negative Poisson ratios over the  $\alpha$ - $\beta$  transition of cristobalite, SiO<sub>2</sub>: a molecular-dynamics study. *Phys. Rev. Lett.* **84**, 5548–5551 (2000).
72. Williams, J. J., Smith, C. W. & Evans, K. E. Off-axis elastic properties and the effect of extraframework species on structural flexibility of the NAT-type zeolites: simulations of structure and elastic properties. *Chem. Mater.* **19**, 2423–2434 (2007).
73. Lee, Y., Vogt, T., Hriljac, J. A., Parise, J. B. & Artioli, G. *J. Am. Chem. Soc.* **124**, 5466–5475 (2002).
74. Lethbridge, Z. A. D., Walton R. L., Marmier, A. S. H., Smith, C. & Evans, K. E. Elastic anisotropy and extreme Poisson's ratios in single crystals. *Acta Mater.* **58**, 6444–6451 (2010).
75. Goodwin, A. L., Keen, D. A. & Tucker, G. Large negative linear compressibility of Ag<sub>2</sub>[Co(CN)<sub>6</sub>]. *Proc. Natl Acad. Sci. USA* **105**, 18708–18713 (2008).
76. Goodwin, A. L. *et al.* Colossal positive and negative thermal expansion in the framework material Ag<sub>2</sub>[Co(CN)<sub>6</sub>]. *Science* **319**, 794 (2008).
77. Mary, T. A., Evans, J. S. O., Vogt, T. & Sleight, A. W. Negative thermal expansion from 0.3 K to 1050 K in ZrW<sub>2</sub>O<sub>8</sub>. *Science* **272**, 90–92 (1996).
78. Bridgman, P. W. *The Physics of High Pressure* (Bell, 1949).
79. Greaves, G. N. & Sen, S. Inorganic glasses, glass-forming liquids and amorphising solids. *Adv. Phys.* **56**, 1–166 (2007).
80. Poole, P. H., Grande, T., Angell, C. A. & McMillan, P. F. *Science* **275**, 322 (1997).
81. Greaves, G. N. *et al.* Detection of first order liquid–liquid phase transitions in yttrium oxide–aluminium oxide melts. *Science* **322**, 566–570 (2008).
82. Hirotsu, S. Elastic anomaly near the critical point of volume phase transition in polymer gels. *Macromolecules* **23**, 903–905 (1990).
83. Lakshtanov, D. L., Sinogeikin, S. V. & Bass, J. D. High-temperature phase transitions and elasticity of silica polymorphs. *Phys. Chem. Miner.* **34**, 11–22 (2007).
84. McKnight, R. E. A. *et al.* Grain size dependence of elastic anomalies accompanying the alpha-beta phase transition in polycrystalline quartz. *J. Phys. Cond. Mat.* **20**, 075229 (2008).
85. Li, C., Hu, Z. & Li, Y. Poisson's ratio in polymer gels near the phase-transition point. *Phys. Rev. E* **48**, 603–606 (1993).
86. Dong, L. Stone, D. S. & Lakes, R. S. Softening of bulk modulus and negative Poisson's ratio in barium titanate ceramic near the Curie point. *Phil. Mag. Lett.* **90**, 23–33 (2010).
87. Alefeld, G., Volkl, J. & Schaumann, G. Elastic diffusion relaxation. *Phys. Status Solidi* **37**, 337–351 (1970).
88. Boehler, R. & Ross, M. Melting curve of aluminum in a diamond cell to 0.8 Mbar: implications for iron. *Earth Planet. Sci. Lett.* **153**, 223 (1997).
89. McMillan, P. F. *et al.* Polyamorphism and liquid–liquid phase transitions: challenges for experiment and theory. *J. Phys. Cond. Mat.* **19**, 415101 (2007).
90. Greaves, G. N. *et al.* Composition and polyamorphism in supercooled yttria–alumina melts. *J. Non-Cryst. Solids* **357**, 435–441 (2011).
91. Inamura, Y., Katayama, Y., Ursumi, W. & Funakoshi, K. I. Transformations in the intermediate-range structure of SiO<sub>2</sub> glass under high pressure and temperature. *Phys. Rev. Lett.* **93**, 015501 (2004).
92. Richet, P. & Gillet, P. Pressure-induced amorphisation of minerals: a review. *Eur. J. Mineral* **9**, 589–600 (1997).
93. Greaves, G. N. *et al.* Rheology of collapsing zeolites amorphised by temperature and pressure. *Nature Mater.* **2**, 622–629 (2003).
94. Greaves, G. N., Meneau, F., Majerus, O., Jones, D. & Taylor, J. Identifying the vibrations that destabilise crystals and which characterise the glassy state. *Science* **308**, 1299–1302 (2005).

95. Haines, J. *et al.* Topologically ordered amorphous silica obtained from the collapsed siliceous zeolite, silicalite-1-F: a step toward “perfect” glasses. *J. Am. Chem. Soc.* **131**, 12333–12338 (2009).
96. Keen, D. A. *et al.* Structural description of pressure-induced amorphisation in  $ZrW_2O_8$ . *Phys. Rev. Lett.* **98**, 225501 (2007).
97. Bennett, T. D. *et al.* Structure and properties of an amorphous metal–organic framework. *Phys. Rev. Lett.* **104**, 115503 (2010).
98. Lethbridge, Z. A. D., Walton, R. I., Bosak, A. & Krisch, M. Single-crystal elastic constants of the zeolite analcime measured by inelastic X-ray scattering. *Chem. Phys. Lett.* **471** 286–289 (2009).
99. Peral, I. & Iniguez, J. Amorphization induced by pressure: results for zeolites and general implications. *Phys. Rev. Lett.* **97**, 225502 (2006).
100. Novikov, V. N. & Sokolov, A. P. Poisson’s ratio and the fragility of glass-forming liquids. *Nature* **431**, 961–963 (2004).
101. Novikov, V. N., Ding, Y. & Sokolov, A. P. Correlation of fragility of supercooled liquids with elastic properties of glasses. *Phys. Rev. E* **71**, 061501 (2005).
102. Jiang, M. & Dai, L. Intrinsic correlation between fragility and bulk modulus in metallic glasses. *Phys. Rev. B* **76**, 054204 (2007).
103. Shintani, H. & Tanaka, H. Universal link between the boson peak and transverse phonons in glass. *Nature Mater.* **7**, 870–877 (2008).
104. Yannopoulos, S. N. & Johari, G. P. Poisson’s ratio and liquid’s fragility. *Nature* **442**, E7–E8 (2006).
105. Scopigno, T., Ruocco, G., Sette, F. & Monaco, G. Is the fragility of a liquid embedded in the properties of its glass? *Science* **302**, 849–852 (2003).
106. Scopigno, T., Cangialosi, D. & Ruocco, G. Universal relation between viscous flow and fast dynamics in glass-forming materials. *Phys. Rev. B* **81**, 100202(R) (2010).
107. Debenedetti, P. G. & Stillinger, F. H. Supercooled liquids and the glass transition. *Nature* **410**, 259–267 (2001).
108. Angell, C. A. Structural instability and relaxation in liquid and glassy phases near the fragile liquid limit. *J. Non-Cryst. Solids* **102**, 205–221 (1988).
109. Dyre, J. C. Colloquium: The glass transition and elastic models of glass-forming liquids. *Rev. Mod. Phys.* **78**, 953–972 (2006).
110. Dyre, J. C. Glasses: Heirs of liquid treasures. *Nature Mater.* **3**, 749–750 (2004).
111. Johari, G. P. On Poisson’s ratio of glass and liquid vitrification characteristics. *Phil. Mag.* **86**, 1567–1579 (2006).
112. Nemilov, S. V. Structural aspect of possible interrelation between fragility (length) of glass forming melts and Poisson’s ratio of glasses. *J. Non-Cryst. Solids* **353**, 4613–4632 (2007).
113. Krisch, M. & Sette, F. in *Light Scattering in Solids: Novel Materials and Techniques* (eds Cardona, M & Merlin, R.) (Springer, 2007).
114. Xi, X. L. *et al.* Fracture of brittle metallic glasses: brittleness or plasticity. *Phys. Rev. Lett.* **94**, 125510 (2005).
115. Pugh, S. F., Relations between the elastic moduli and the plastic properties of polycrystalline pure metals, *Phil. Mag.* **45**, 823–843 (1954).
116. Rosenhain, W. & Ewen, D. The intercrystalline cohesion of metals. *J. Inst. Met.* **10**, 119–149 (1913).
117. Zhang, H., Srolovitz, D. J., Douglas, J. F & Warren, J. A. Grain boundaries exhibit the dynamics of glass-forming liquids. *Proc. Natl Acad. Sci. USA* **106**, 7735–7740 (2009).
118. Greer, A. L. Metallic glasses. *Science* **267**, 1947–1953 (1995).

### Acknowledgements

We acknowledge support from the Higher Education Funding Council for Wales, the Engineering and Physical Sciences Research Council (UK), the Natural Environment Research Council (UK), the National Science Foundation (USA), and the Ministry of Research and Higher Education in France. We are also indebted to J. Grima, T. Kelly, C. Kukijan, J. Orava, R. Reis and R. Walton for discussions in the preparation of this Review.

### Additional information

The authors declare no competing financial interests.